

CHAPTER 4

RESULTS AND DISCUSSION

4.0 Results and Discussion

4.1 Purification of MWCNTs

Purification of carbon nanotubes has attracted a great deal of attention because some applications require high purity material. Carbon nanotubes are usually contaminated with metal catalyst, metal support, amorphous carbon and graphitic nanoparticles. The presences of these impurities have been shown to obstruct their application (Hu et al., 2003). The purification method by refluxing nanotubes in nitric acid is the most often employed in many applications. The major function of nitric acid treatment is to remove metal catalyst together with amorphous carbon by the oxidation process. Figure 4.1 shows the EDX spectrum of the (a) Pristine MWCNTs (b) Purified MWCNTs.

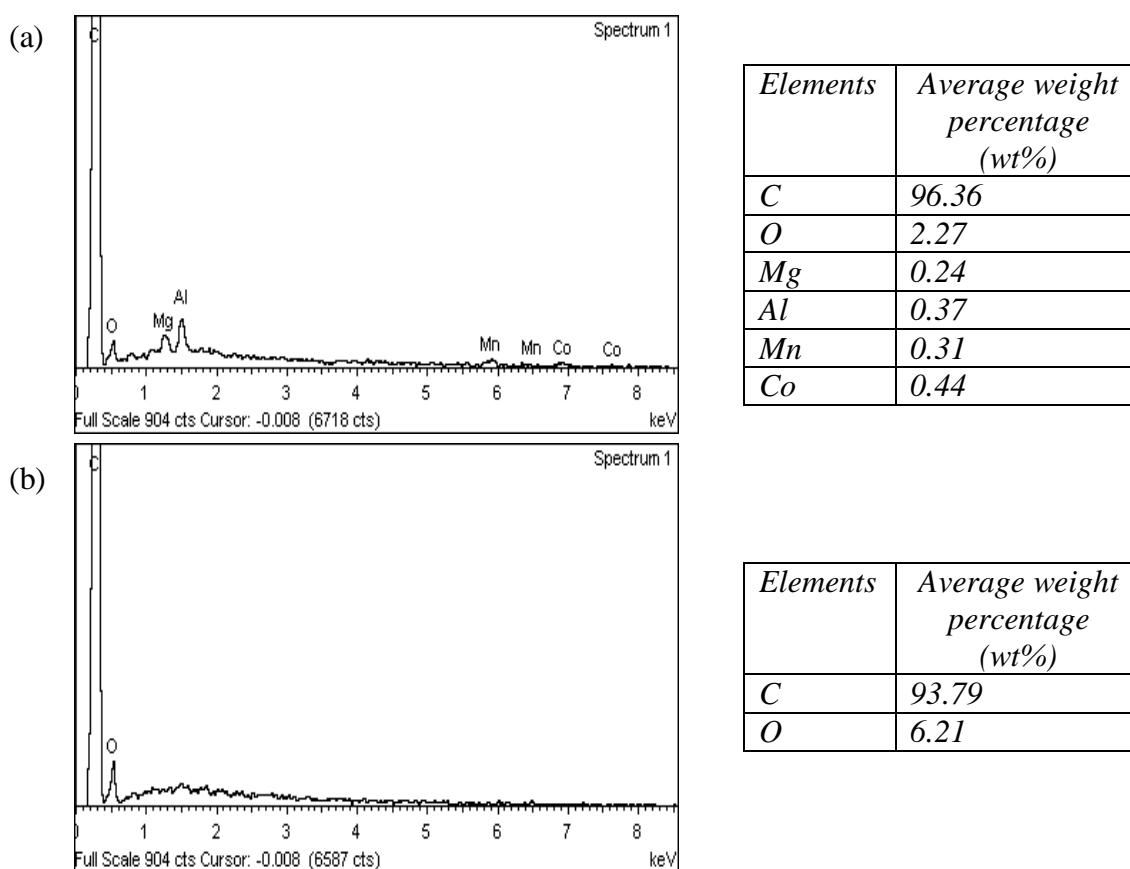


Figure 4.1: The EDX spectrum of the (a) Pristine MWCNTs (b) Purified MWCNTs.

The EDX analysis detected small amounts of metals such as Magnesium, Aluminium, Manganese and Cobalt from residual catalyst in the pristine MWCNTs sample. After the purification process, all the metal catalysts and support have been successfully removed. The percentage of oxygen detected increased from 2.27 to 6.21 %. This is likely due to carbon atoms on the surface of MWCNTs have been oxidized by the nitric acid treatment.

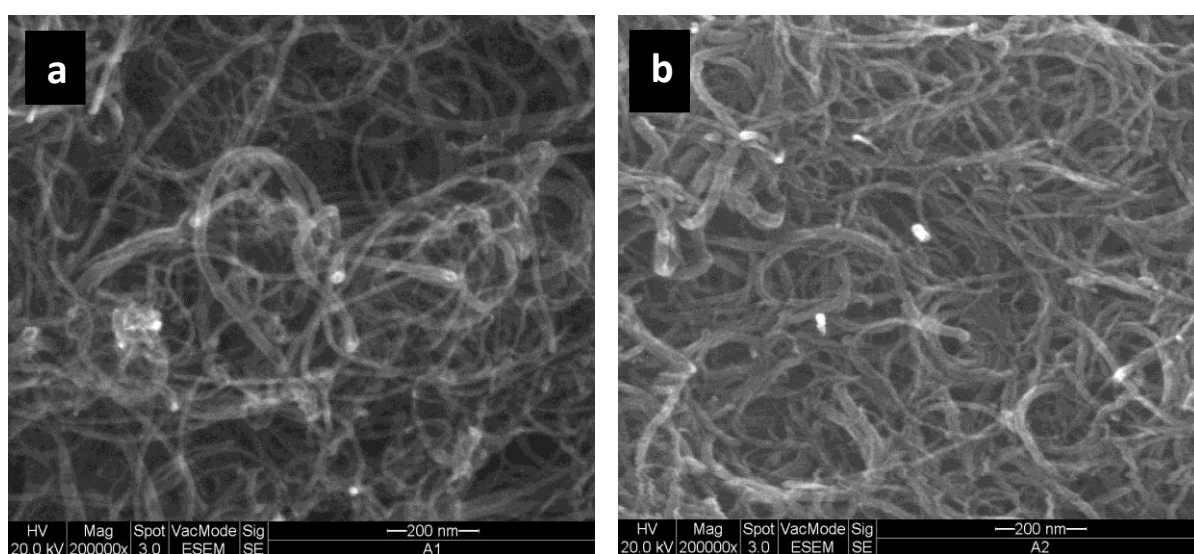


Figure 4.2: The SEM images of (a) Pristine MWCNTs (b) Purified MWCNT

Figure 4.2 shows the SEM images of pristine and purified MWCNTs. There were no significant changes in the shape of MWCNTs before and after purification. The high degree of entanglement was found for both samples.

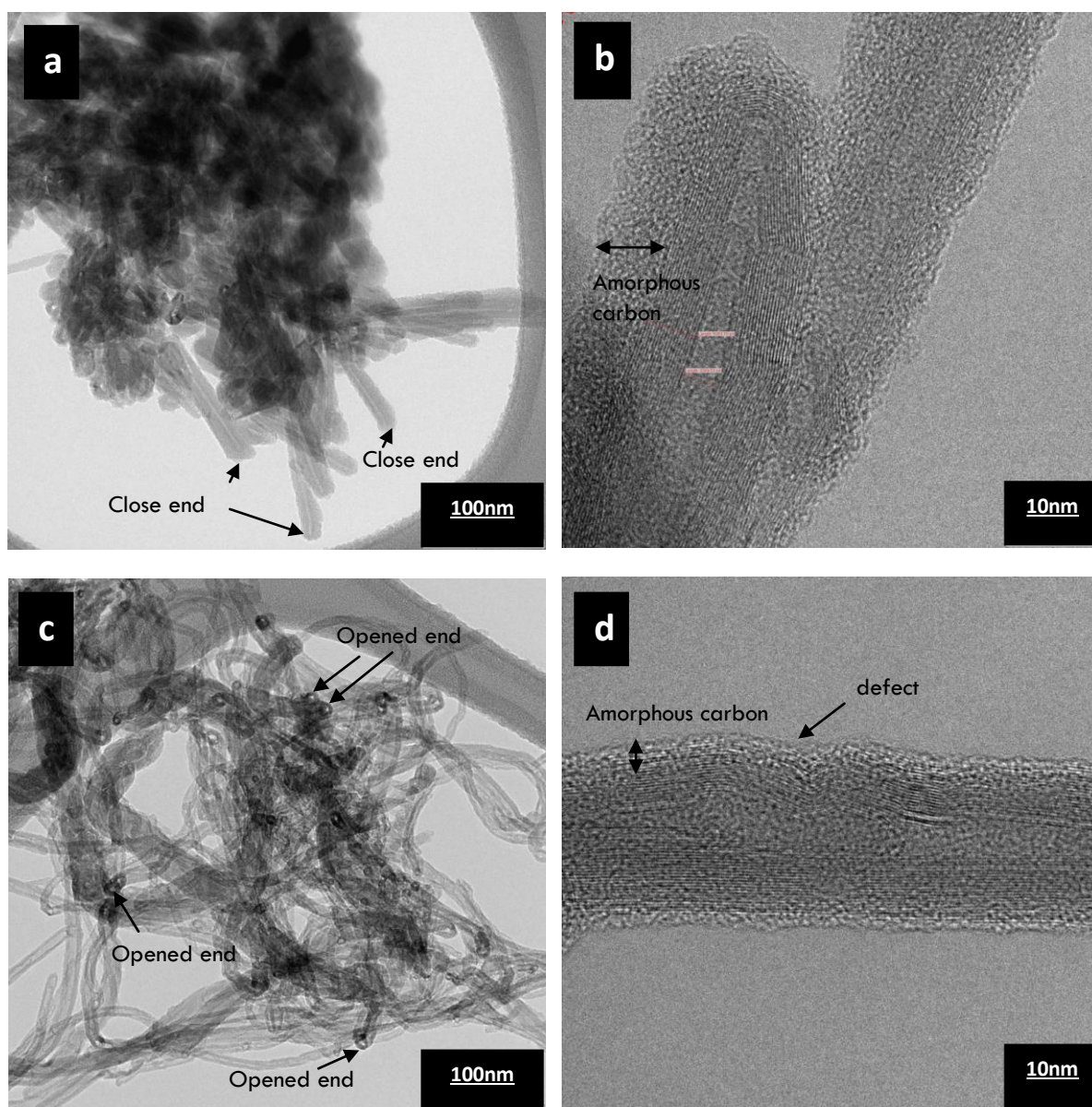


Figure 4.3: The TEM images of (a) agglomerated Pristine MWCNTs (b) Pristine MWCNTs shows the thick amorphous carbon (c) MWCNTs were loosely packed and showed open end after purification process (d) Purified MWCNTs shows reduced thickness of amorphous carbon

The TEM images of pristine and purified MWCNTs are shown in Figure 4.3. Figure 4.3 (a) shows agglomerated pristine MWCNTs due to high hydrophobicity properties of these tubes. Figure 4.3(b) shows the presence of a thick layer of amorphous carbon on the outer surface layer of pristine MWCNT samples. After the purification process with nitric acid, the MWCNTs were loosely packed and open end of MWCNTs were created, see Figure 4.3 (c). Beside, the outer wall surface of the purified MWCNTs becomes smoother, see Figure 4.3(d). This is due to the removal of most amorphous carbon on the outer wall surface of sample. Besides, purification has also created surface defects. As shown in Figure 4(d), there are some defects created on the outer layer wall of purified samples.

4.2 Surface Acidity

The results presented in Figure 4.4 and Table 4.1 show the titration profile of the gas phase functionalized samples. The profile of the titration curves for samples B7 and B8 are almost similar. The B6 sample, which was treated at 100 °C, clearly contains two distinctive peaks that were detected in NaOH filtrate. This implies the presence of two types of functional groups. In contrast, B7 and B8 (treated at 200 and 300 °C respectively) shows two peaks that cannot be resolved well, possibly due to degree of oxidation at high temperature which generates molecular oxidation debris on the carbon surfaces. The oxidative treatment of CNTs leads to erosion of their structure. It was observed that as the shortening and thinning of the CNT layer occurs, carbonaceous debris was produced (Wang et al., 2009).

From the first derivative order of the titration profile, the two indistinctive peaks can also be assumed due to the presence of two different functional groups on the

surfaces of the samples. The equivalent point was reached when the moles of base added equals the moles of acid in the samples. This point can be used to determine the number of acidic sites in the samples. As shown in Table 4.1, the first acid dissociation constant (pK_{a1}) of B6, B7 and B8 have values of 3.34, 3.50 and 4.02 respectively, can be assigned as dicarboxylic, an acid group which is one of carboxylic members. These pK_a values were in very good agreement with values reported by Murakami and co-workers, where the acid dissociation constant of dicarboxylic acid was about 3.8 which were assigned as carboxyl groups. The first and second acid dissociation constants of dicarboxylic acid are 1.7 – 4.5 and 4.1 – 5.8 respectively (Murakami et al., 2003).

The B6 sample shows second acid dissociation constant (pK_{a2}) value of 5.98 which might be related to high numbers of lactone groups. The second acid dissociation constant (pK_{a2}) of 7.1 for B7 and 7.0 for B8 can be assigned as phenolic and lactone groups, respectively. The result shows acidic sites created with different acid dissociation constants (K_a) values. The magnitudes of the K_a and pK_a values of different acid give the comparison of their relative strength.

As reported by Barkauskas and Dervinyte, the surface functional groups were divided into carboxyl ($pK_a = 2.0- 4.0$), lactone ($pK_a = 4.0 – 7.0$) and phenol ($pK_a = 7.0 – 10.0$) (Barkauskas & Dervinyte, 2004). The acidic sites with $pK_a < 8$ corresponded to carboxylic or lactone and acidic sites with $pK_a > 8$ corresponded to phenolic groups (Puziy et al., 2001). They also reported that the acidic sites with pK_a value around 3.5 – 3.9 may be assigned to carboxylic groups, the groups with pK_a value around 7.7 – 8.0 may be connected to phenolic groups and the groups with pK_a around 5.3 – 5.9 may be related to hydroxyl groups. From the results, the samples treated at 200 °C (B7) shows

the lowest pK_{a1} value and highest pK_{a2} values as compared to B6 and B8 samples which were treated at 100 and 300 °C. This might be due to the high degree of oxidation which creates high amount of carboxylic functional group on the carbon surfaces and the high value of pK_{a2} results from a small amount of phenolic group which were created on the surfaces. Thus, more strong acidic groups need more volume of NaOH to neutralize the surfaces. Since the B7 sample consumes more volume of NaOH thus the amounts of acidic sites were significantly higher than other treated samples of $6.05 \times 10^{-4} \text{ mol.g}^{-1}$. The amount of acidic sites for the B6 sample was $4.36 \times 10^{-4} \text{ mol.g}^{-1}$. This is lower than B7 due to the low treatment temperature. This implies that less number of functional groups were created on the surfaces. Sample treated at higher temperature of 300 °C suggests lower number of acidic site created on the carbon surface.

Table 4.1: Total number of acidic functional groups and pKa values for functionalized MWCNTs samples

Treatment	pKa values		Total number of surface acidic functional groups (mol.g^{-1})	Functional group present
	pK_{a1}	pK_{a2}		
B6	3.50	5.98	4.36×10^{-4}	Carboxyl and Lactone
B7	3.34	7.10	6.05×10^{-4}	Carboxyl and Phenol
B8	4.02	7.00	2.70×10^{-4}	Carboxyl and Lactone
B9	3.71	-	1.95×10^{-4}	Carboxyl
B10	3.82	-	2.02×10^{-4}	Carboxyl
B11	4.05	-	1.28×10^{-4}	Carboxyl

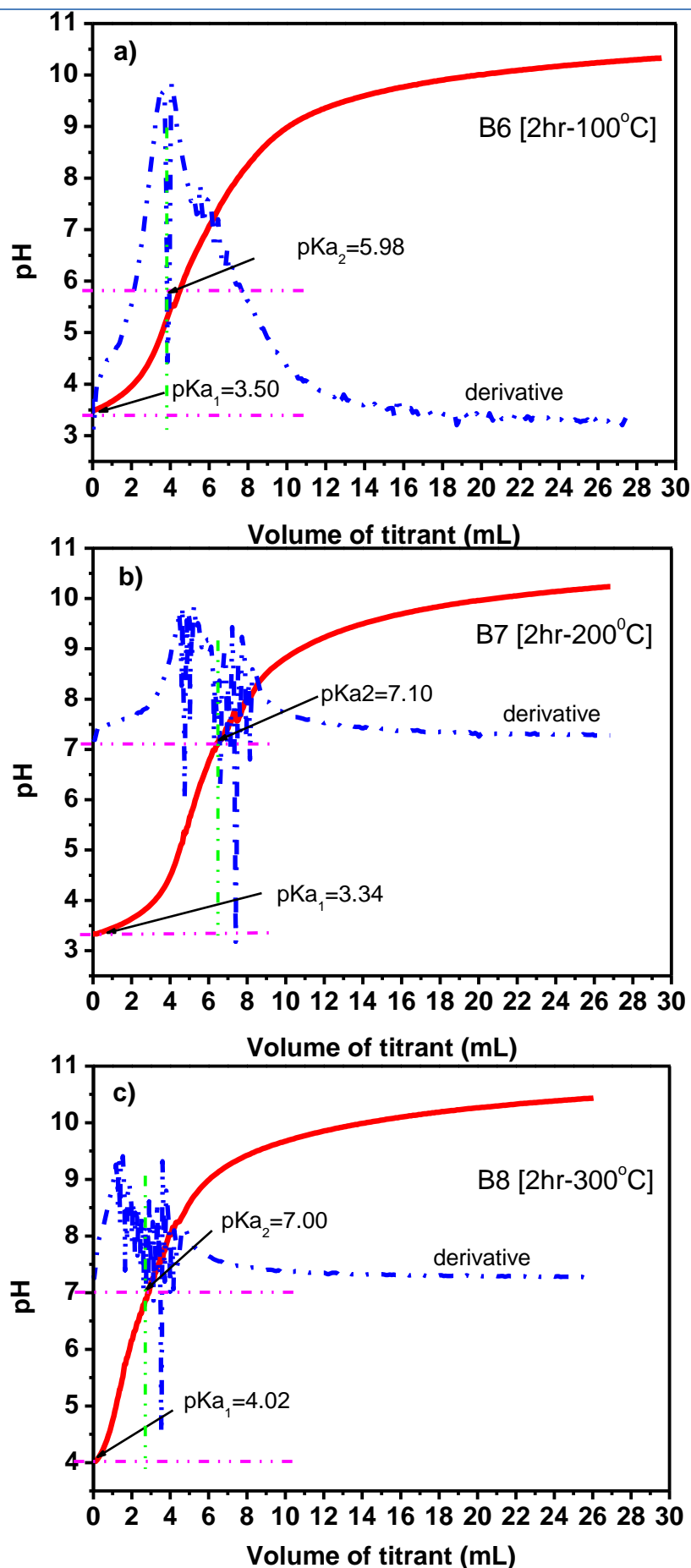


Figure 4.4: The acid base titration profile for (a) B6 (b) B7 (c) B8

The titration profiles for the liquid phase functionalization samples are presented in Figure 4.5 (a), (b), (c) and Table 4.1. In general, the total numbers of acidic functional groups created on the surface of the liquid phase treated samples are lower than the gas phase treated samples. The B9 sample that was treated at 100 °C has a total number acidic functional group of $1.95 \times 10^{-4} \text{ mol.g}^{-1}$. The titration profile of 1st derivative of this sample shows the single peak with small shoulder indicating the inflection point at pH 5.86, see Figure 4.5(a). At this point the volumetric equivalent was reached between the moles of base and the moles of acid in the sample. The B10 sample that was treated at 200 °C also shows a single peak with the total acidic functional group of $2.02 \times 10^{-4} \text{ mol.g}^{-1}$. The volumetric equivalent reached at the point where the maximum peak of the 1st derivative crossing the titration peak located at pH 6.42, see Figure 4.5(b). From the 1st derivative titration profile, a clear single peak was observed for sample that has been treated at 300 °C (B11). The volumetric equivalent point of titration was reached at pH 7.04 that gave the total number of acidic functional group of $1.28 \times 10^{-4} \text{ mol.g}^{-1}$, see Figure 4.5(c).

Single peak was observed for all liquid phase (B9, B10 and B11) samples, indicating the presence of only carboxylic functional group on the surface of functionalized carbon with the pKa values of 3.17, 3.82 and 4.05 respectively (Puziy et al., 2001; Barkauskas & Dervintyl, 2004). The B10 sample exhibits the highest number of acidic functional group for the liquid phase treatment. From all gas and liquid phase samples, it was found that the treatment temperature at 200 °C is the optimum temperature that creates highest number of acidic site on the carbon surface. At this temperature, the gas phase sample (B7) exhibited the highest number of acidic site as compared to liquid phase treatment (B10) samples.

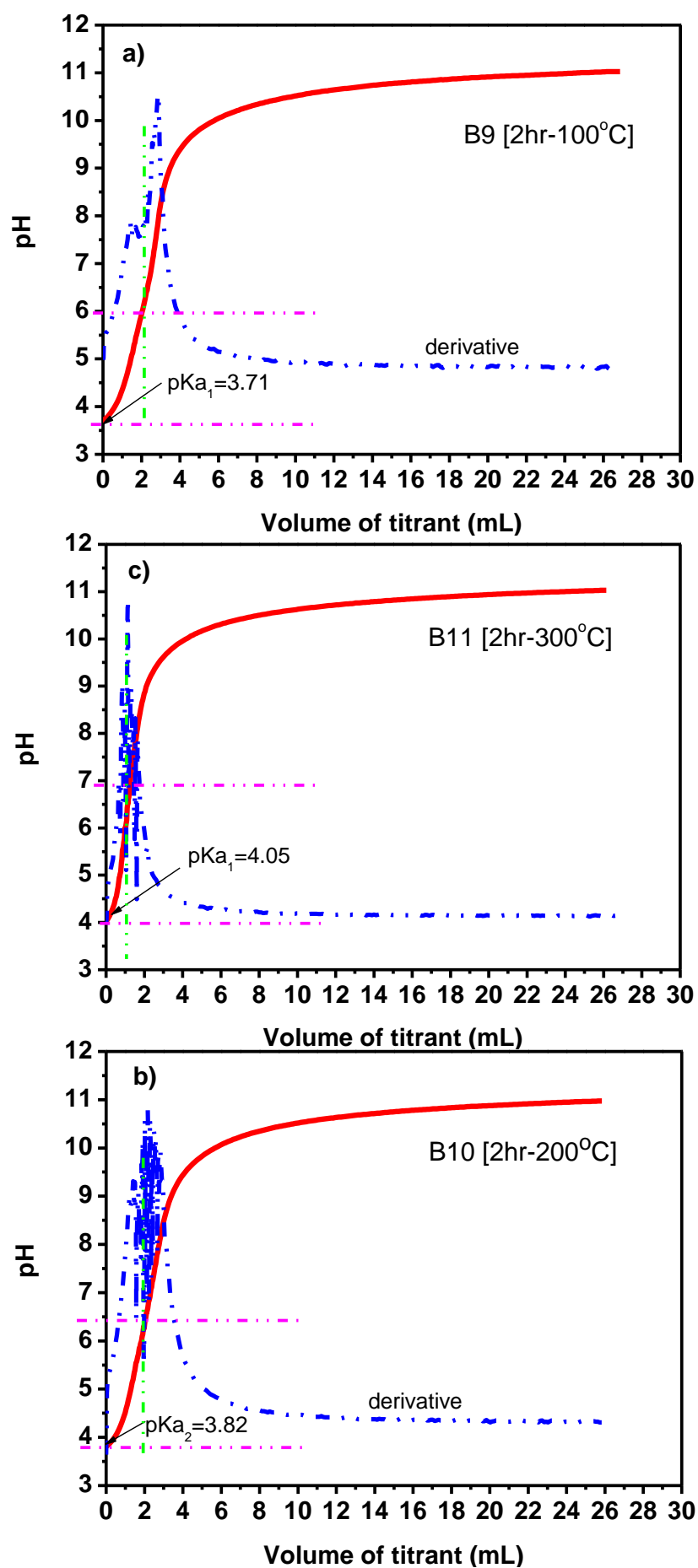


Figure 4.5: The acid base titration profile for (a) B9 (b) B10 (c) B11

4.3 Thermal stability

Thermal behaviour of the functionalized samples were measured by thermogravimetric analysis. Figure 4.6 (a) and 4.6 (b) are the TGA curves of the gas phase and liquid phase functionalized samples in the range of 30 – 1000 °C. Figure 4.6 (a) shows the functionalized samples of B6 and B7 decompose in three distinct steps which are at 30 – 200 °C, 200 – 300 °C and 300 – 1000 °C. Both the samples (B6 and B7) exhibit almost the same TGA curve. The first, second and third weight loss detected were about 0.5 %, 2.0 % and 4.0 %, respectively for both samples. In contrast, B8 exhibits two region of decomposition at onset temperatures of 30 – 400 °C and 400 – 1000 °C with weight loss of 0.5 % and 3.0 % respectively. This result indicates the high thermal stability of the samples. The TGA results of gas phase were in good agreement with the amount of acidic functional groups determined from the acid base titration observation.

Figure 4.6 (b) shows the diagram of liquid phase functionalized samples of B9, B10, and B11. They indicate that the decomposition occurs in three distinct steps which are at 30 – 300 °C, 300 – 700 °C and 700 – 1000 °C. The samples B10 and B11 exhibit similar TGA curves. The first weight loss detected for B9, B10 and B11 were about 0.2, 0.4 % and 1.0 %, respectively. The second weight loss for B9, B10 and B11 were about 3.0, 2.6 and 2.8 % respectively. The third weight loss for B9, B10 and B11 were about 8.9, 5.3, and 5.0 % respectively.

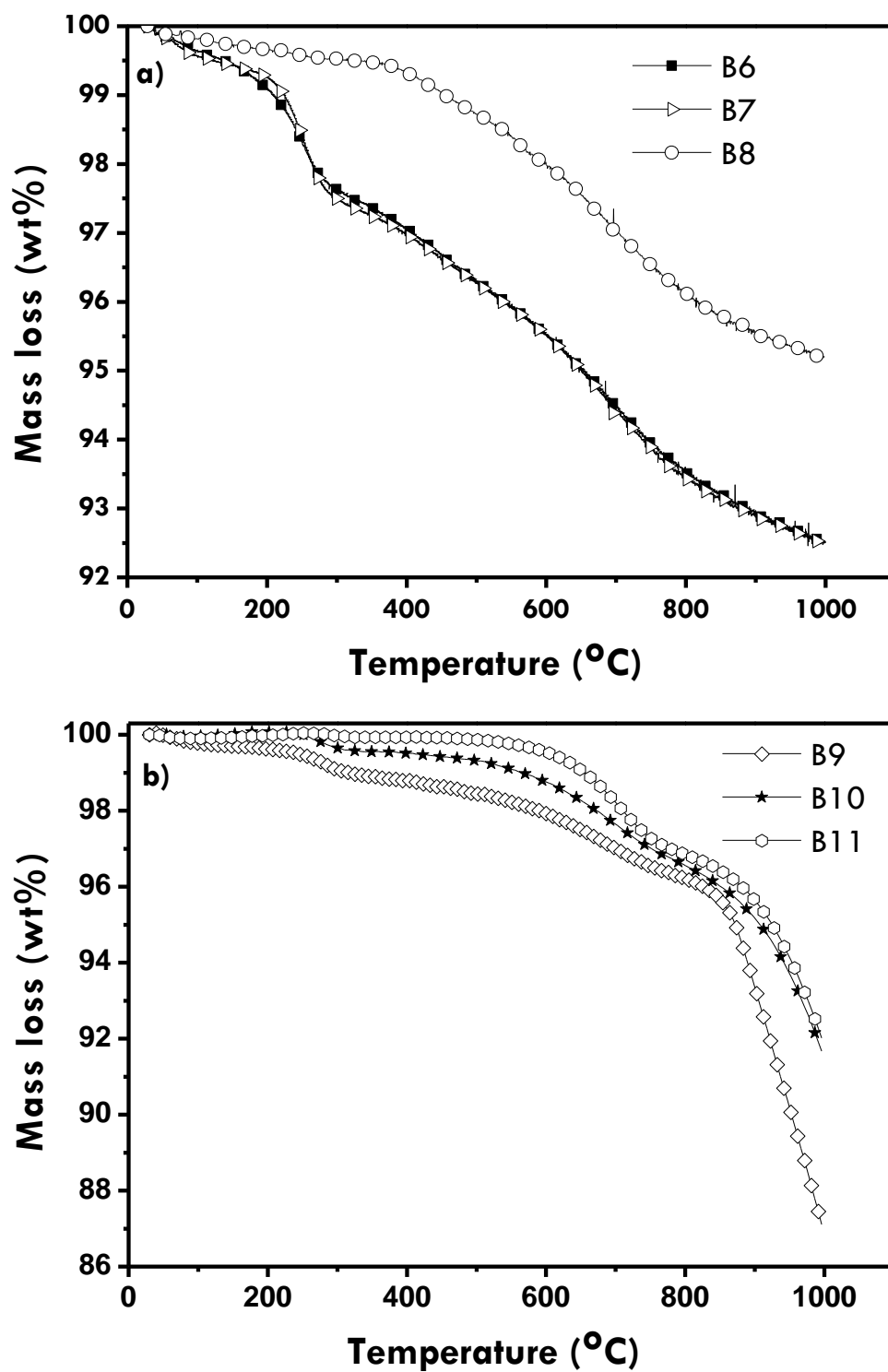


Figure 4.6: Thermogravimetric curve of (a) gas phase (b) liquid phase functionalized samples.

Figures 4.7 (a), (b) and (c) show the mass spectroscopy (MS) fragment ion curves for B6, B7 and B8 functionalized samples, respectively. The MS ion curves for water (m/z 18), CO (m/z 28), CO₂ (m/z 44), SO (m/z 48) and SO₂ (m/z 64) display peaks that correspond closely to the individual steps in the TGA curves. The similar MS ion curve for B6 and B7 is shown in Figures 4.7(a) and 4.7(b). As shown in the curve, the first mass loss step of B6 and B7 relates to the elimination and vaporization of water about 100 °C. The second step is due to the decomposition of carboxylic and anhydrides group such as sulphur and oxygen containing functional groups with the formation of SO₂, SO, CO₂ and small amount of CO gaseous. The third step shows the evolution of high amounts of CO₂ and CO due to decomposition of lactone and phenol groups which is thermally stable as compared to carboxylic and anhydrides groups. As shown in Figure 4.7(c), the sample B8 shows two steps of decomposition. The first step shows the evolution of SO₂ and SO gaseous together with vaporization of a small amount of water of crystallization. The second step shows the evolution of CO₂ and CO gaseous. This functionalized sample was thermally stable as compared to B6 and B7

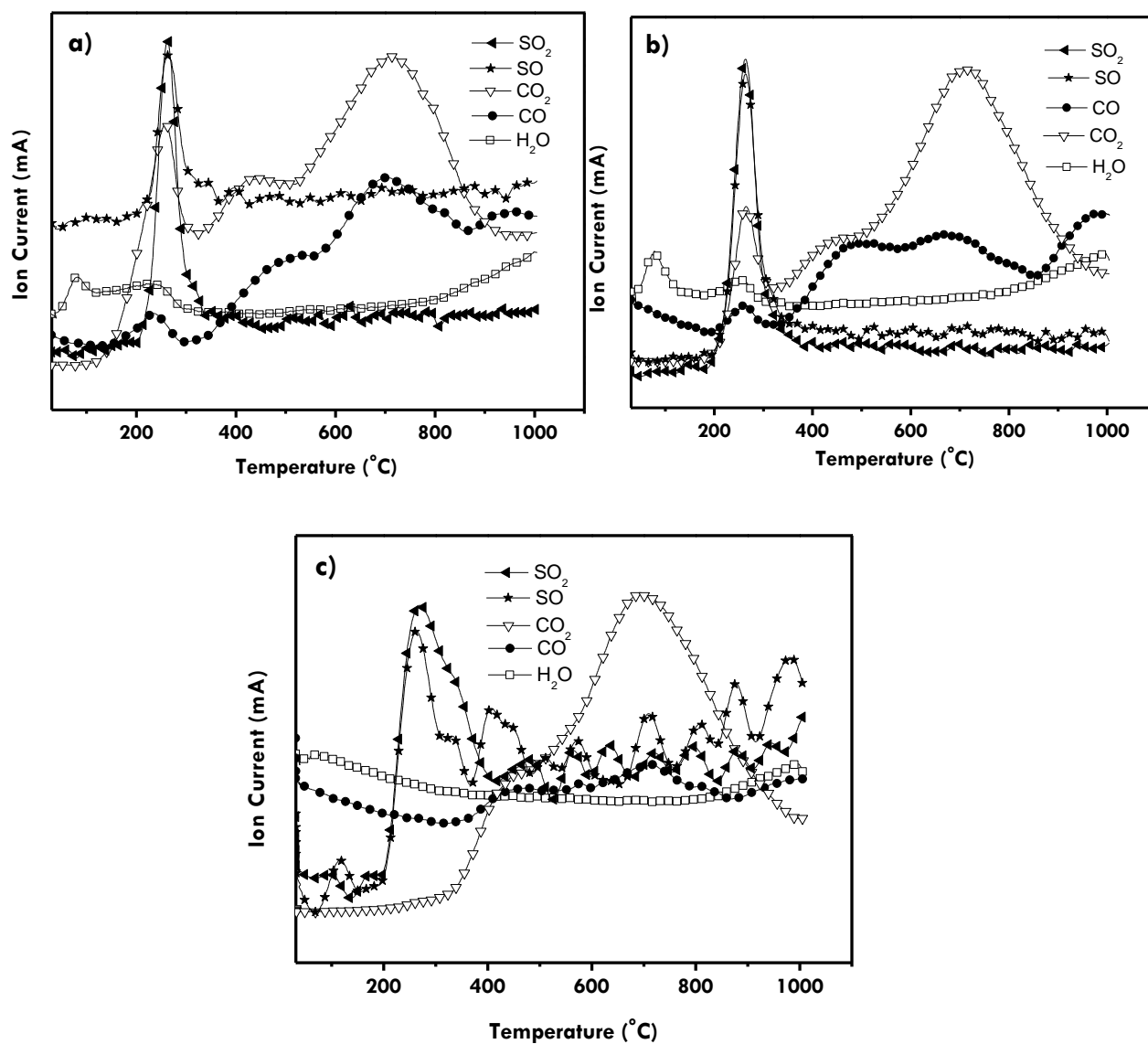


Figure 4.7: Mass spectroscopy of gas phase functionalized sample (a) B6, treated at 100 °C for 2hrs (b) B7, treated at 200 °C for 2 hrs (c) B8, treated at 300 °C for 2 hrs.

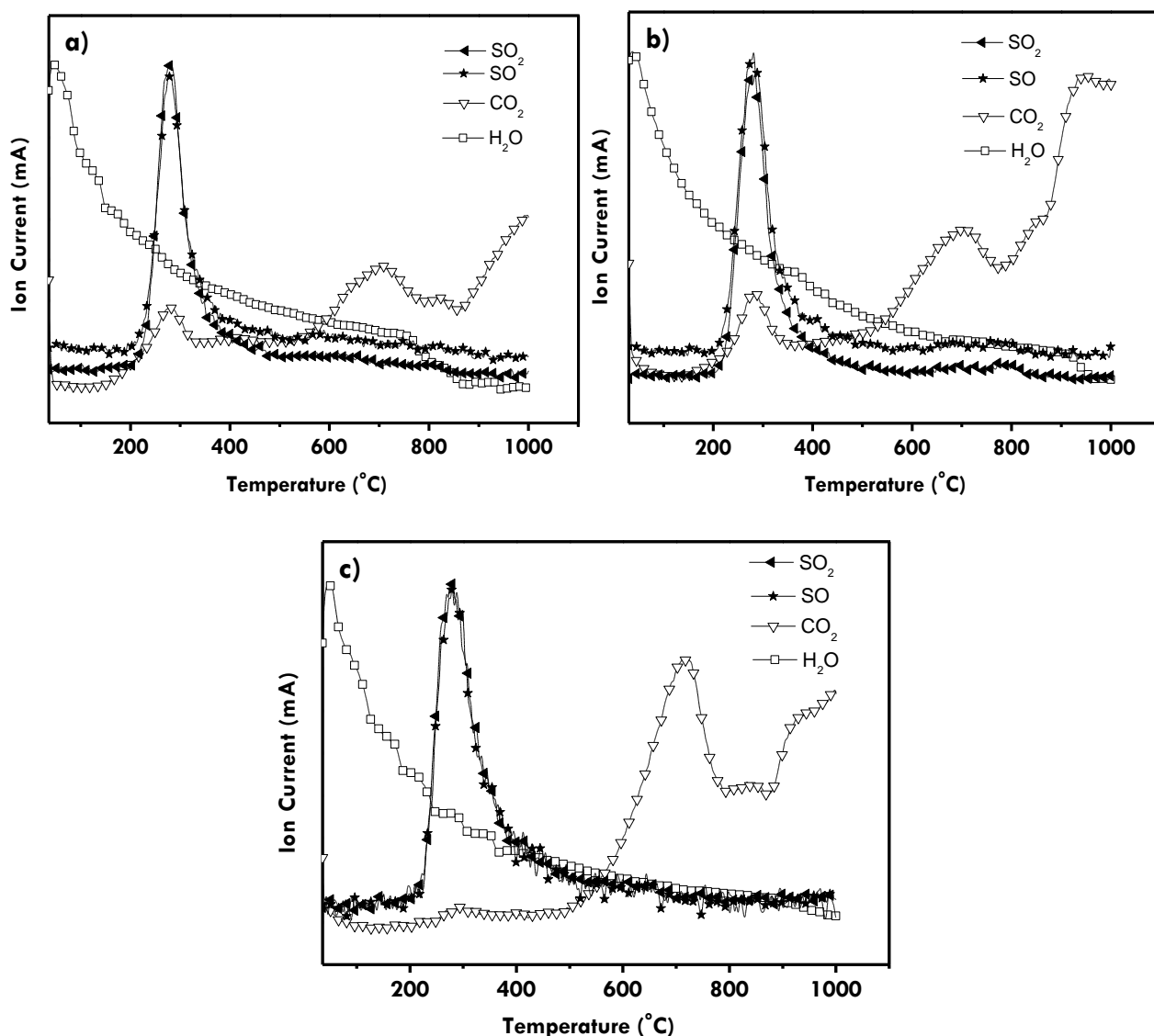


Figure 4.8: Mass spectroscopy of liquid phase functionalized sample (a) B9, treated at 100 °C for 2hrs (b) B10, treated at 200 °C for 2 hrs (c) B11, treated at 300 °C for 2 hrs.

Figure 4.8 (a), (b) and (c) shows the mass spectroscopy (MS) fragment ion curves for B9, B10 and B11 liquid phase functionalized samples, respectively. The MS ion curves show all samples (B9, B10 and B11) decompose high amount of water at about 100 °C. This due to the treatment is in liquid phase system. While the TGA curves for B10 and B11 are similar, see Figure 4.6(b), the MS ion curves are slightly different in the evolution of CO₂, see Figure 4.8(b) and 4.8(c), respectively. All samples show the decomposition of SO₂, SO and CO₂ gaseous at second step of weight loss

(300 – 700 °C). But for B11, low amount of CO₂ evolved at about 300 °C and high amount at high temperature of 700 °C. The continuous decomposition of CO₂ gases was observed as the temperature increases to 1000 °C. There are no CO gases observed in the liquid phase samples as compared to gas phase samples.

4.4 Functional groups Identification

Attenuated Total Reflectance Infrared (ATR-IR) spectroscopy was carried out to identify the functional groups present on the sidewall of the functionalized samples. The Infrared (IR) spectra of pristine and purified MWCNTs are shown in Figure 4.9. Both IR spectrums show almost the same pattern of transmittance band. The detectable strong transmittance bands at 1080 cm⁻¹ can be assigned to C-O stretching group. The small peak at 1384 cm⁻¹ is attributed to C-H bending group. The weak transmittance band at 1574 cm⁻¹ can be attributed to the carbon skeleton. In addition, the weak transmittance band at 2917 cm⁻¹ and 2849 cm⁻¹ can be assigned to C-H stretching mode. The broad transmittance band centered at 3434 cm⁻¹ corresponds to the hydrogen bond –OH (Chen et al., 2008). There is no significant change in the functional group created on the carbon surfaces between pristine and purified sample.

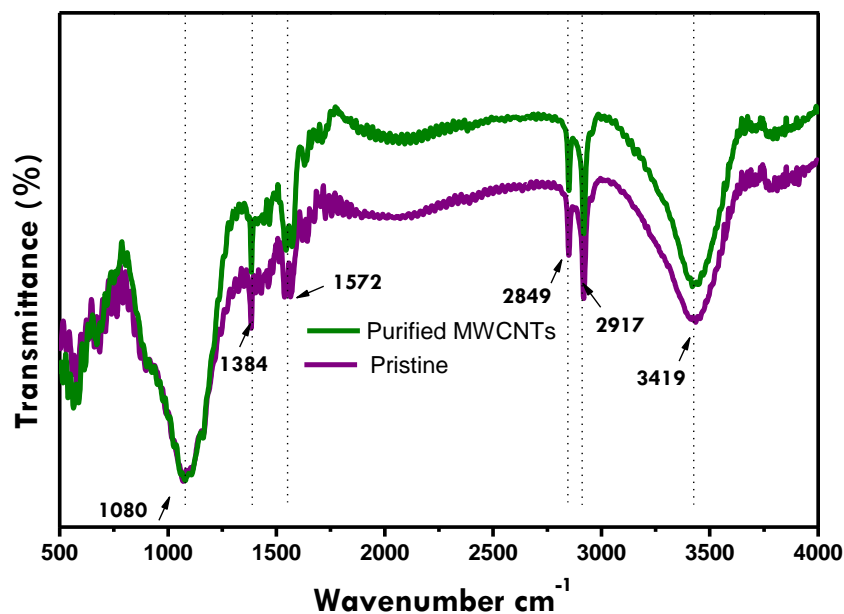


Figure 4.9: IR spectra of pristine and purified MWCNTs.

The IR transmittance bands of gas phase functionalized samples are shown in Figure 4.10 (a). Samples that were treated at 200 °C (B7) and 100 °C (B6), show the medium peak at 3720 cm⁻¹. While sample that was treated at 200 (B7) and 300 °C (B8) has a weak peak at 3785 cm⁻¹. This indicates the presence of unbounded or free hydroxyl group (-OH) of phenol which usually adsorbs strongly in the range of 3650 – 3584 cm⁻¹ region (Nyquist, 2008). This is in contrast with the intermolecular hydrogen bonded OH:OH frequency which occurs at lower frequency 3200 – 3400 cm⁻¹ (Nyquist, 2008; Naseh et al., 2009). The broad weak line at 3175 and 3365 cm⁻¹ is due to the presence of intermolecular hydrogen bonding indicating the characteristic of the O-H stretch from phenolic group (C-OH). At this peak, B7 sample showed the broadest IR absorption than two other samples (B6 and B8). This indicates that the phenolic group dominate in B7 sample. This result was consistent with the pK_a value of functional groups determined from the acid base titration method. The B7, B8 and B6 showed the strong, medium and weak transmittance band at 2353 cm⁻¹. This indicates the presence

of CO and CO₂ groups. Apparently, a CO and CO₂ group originally exhibits the spectrum in the range of 2100 to 2400 cm⁻¹ (Owens & Poole, 2008).

The IR spectrum of B7 shows a strong peak at 1702 cm⁻¹ while B6 and B8 show a weak and medium peak, respectively. This line spectra was assigned to the C=O stretching mode of the carboxylic groups (-COOH) (Naseh et al., 2009). The strong transmittance band observed from the B7 sample might be due to the strong oxidation by SO₃ vapor that creates more carboxylic groups on the carbon surfaces at treatment temperature of 200 °C. In contrast, a weak peak was observed for the B6 sample. This is possibly due to the low number of carboxylic group created on the sidewall of the functionalized sample that was treated at 100 °C. At low temperature of acid treatment, the low degree of acid dissociation created low number of acidic sites on the surface of the functionalized samples. It was reported that refluxing or sonicating CNTs in nitric acid and another strong oxidant such as sulfuric acid opens the ends of the CNTs and introduces carboxylic groups at the open ends and at defect side on the CNTs (Hu et al., 2003).

Meanwhile, the medium peak observed at 1702 cm⁻¹ for B8 might be due to the decomposition of carboxylic group at higher temperature of 300 °C. It is well documented that the carboxylic acid groups are least stable and typically decompose at temperatures below 600 °C (Tessonier et al., 2009). Generally, it is well known that the carboxylic groups with strong acidity have tendency to appear at lower wavenumbers (Murakami et al., 2003). The peak at 1540 cm⁻¹ refers to the C=C stretching mode which originates from the backbone of carbon nanotubes. The similar feature of transmittance band was reported by Naseh et al., 2009 and Yu et al., 2008.

The sample that has been treated at 200 °C, B7, shows a strong line at 1125 cm⁻¹ indicating SO₂OH or R-SO₂O⁻ groups representing the SO₂ symmetric stretching mode. This line probably results from the formation of sulfonate groups on carbon surfaces (Silverstein & Bassler, 1991). There was almost no transmittance band at 1125 cm⁻¹ for samples B6 and B8. This might be due the low number of acidic site and sulphur molecules created on the functionalized carbon surfaces.

The weak transmittance band at 1011 cm⁻¹ only detected for B7 is C-S stretching mode possibly due to the presence of thiolcarbony group. Samples also showed a peak at 860 cm⁻¹ which can be assigned to S-O-C stretching groups. In low frequency range, the peak at 770 cm⁻¹ and 695 cm⁻¹ was related to S-C-H stretching mode, suggesting the existence of sulfonic acid groups. The S-C-H group is less polar than the C-O group and has a considerably weaker bond. Therefore, the band is not intense and it falls at lower frequencies. In fact the stretching vibration assigned to S-C-H linkage occurs in the region of 700 – 600 cm⁻¹ (Silverstein & Bassler, 1991).

The liquid phase treated samples of IR transmittance band are shown in Figure 4.10(b). Liquid phase samples show less detectable peak than gas phase samples. Samples that were treated at 100 °C (B9) and 300 °C (B11) show strong broad peak at 3433 cm⁻¹. While sample that was treated at 200 °C (B10) show weak broad peak at the same wavenumber. This strong broad peak indicates the presence of hydroxyl group (-OH) probably the most dominant characteristic in carboxyl groups (O=C-OH) (Chen et al., 2008). A similar peak also appeared from the pristine and purified MWCNTs samples, but had a small shift in the wavenumber. This peak was contributed by the intermolecular hydrogen bonded OH:OH (Nyouist, 2001; Naseh et al., 2009). Besides,

this peak was not detected in the gas phase sample indicating the hydroxyl group only created in liquid phase treatment sample.

The sharp weak peak at 2918 cm^{-1} and 2850 cm^{-1} result from the C-H stretching mode. The weak peak seen at wavenumber of 1703 cm^{-1} for all samples can be assigned as C–O stretching mode of the carboxylic groups. This peak shows very weak transmittance band as compared to the similar peak in the gas phase treated samples. This might be due to the small amount of carboxylic groups anchored on the carbon surface in the liquid phase treatment. The peak at 1554 cm^{-1} referred to the C=C stretching mode of carbon skeleton. The weak transmittance band at 1426 cm^{-1} can be interpreted to the characteristic of the hydroxyl bond O–H bend. The strong peak at 1097 cm^{-1} can be assigned to C–O–C stretching of carboxylic group (Chen et al., 2008).

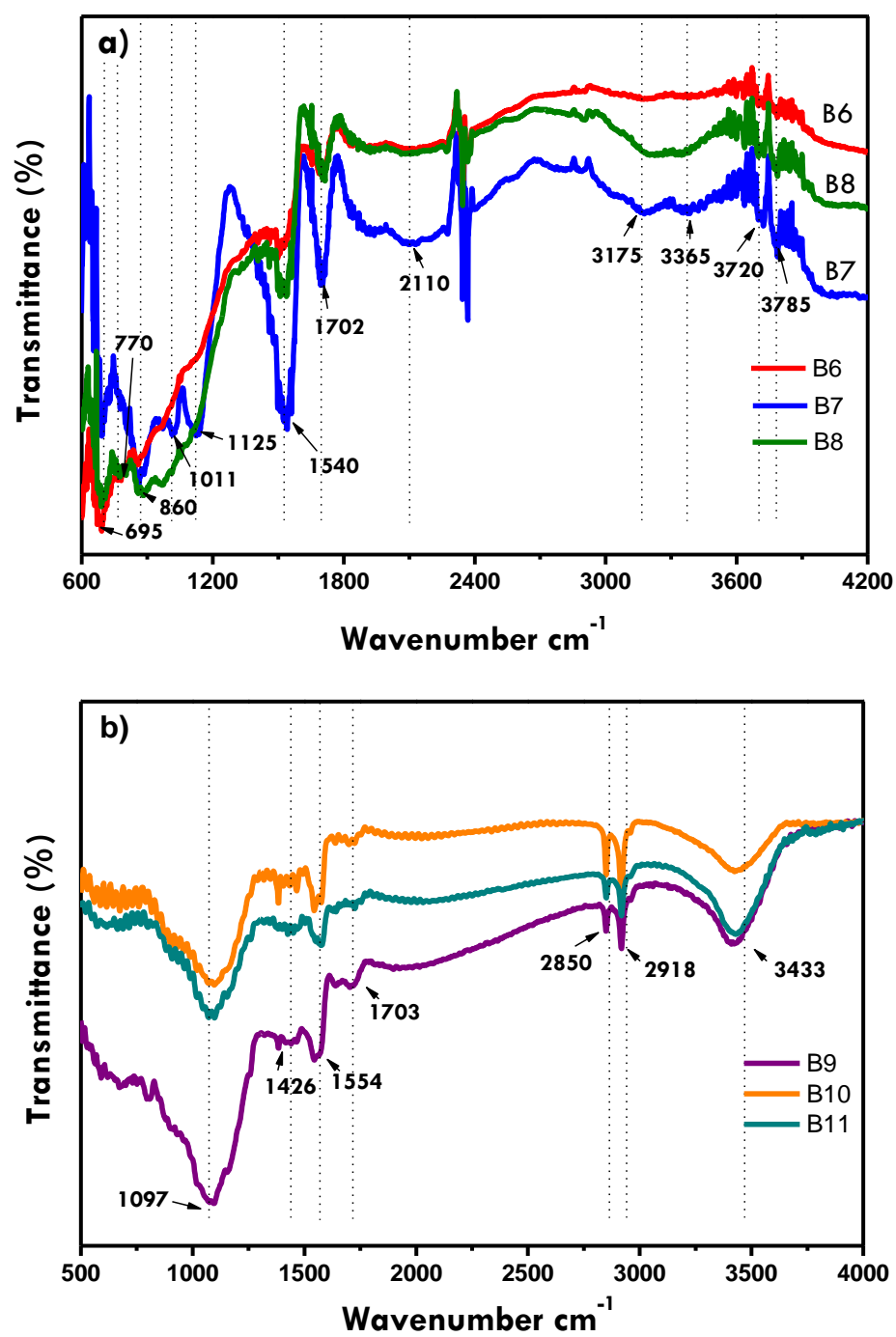


Figure 4.10: IR spectra of (a) gas phase (b) liquid phase functionalized samples.

4.5 Powder X-ray diffraction

The variation of the graphitic character of MWCNTs samples were investigated by X-ray powder diffraction (XRD). X-ray diffraction patterns of pristine and purified MWCNTs are shown in Figure 4.11. The pristine and purified sample exhibits almost the same x-ray diffraction patterns. However, the peak (002) at 2θ values of 25.5° for purified MWCNTs seems slightly more intense as compared to pristine sample. This indicates that the order of graphitic character has been increased by the purification treatment.

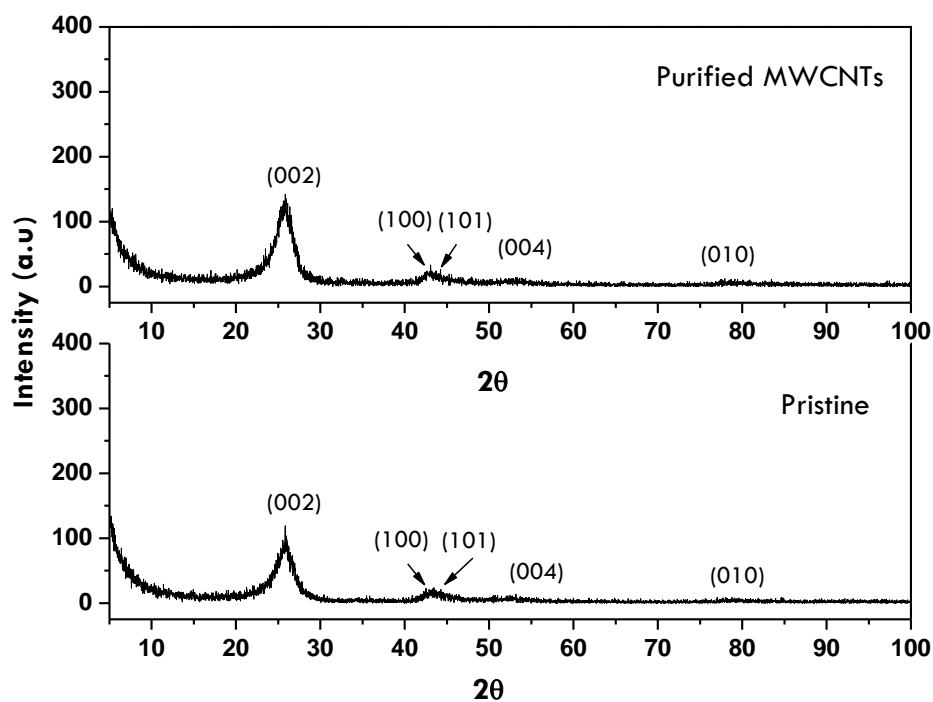


Figure 4.11: X-ray diffraction patterns of pristine and purified MWCNTs.

The XRD pattern of gas and liquid phase treated samples are presented in Figure 4.12. The result shows the presence of hexagonal graphite peak (002) at 25° . The graphite broad peak at 43° can be assigned for both hexagonal (100) and rhombohedral (101) as the two peaks is between 42° and 44° . The liquid and gas phase treatment

seem to increase the intensity of the diffraction peak (004) at 54° and peak (010) at 78° . The peak at 54° was assigned to hexagonal graphite.

Peak at 78° was contributed by rhombohedral graphite. These peaks correspond to the graphite-2H and graphite-3R, respectively. Similar results have been reported by Tessonnier and co-workers (Tessonnier et al., 2009). Liquid phase treated samples show the highest intensity of x-ray diffraction than the gas phase treated samples, see Figure 4.12(b). This might be due to the fewer defects created on the wall layer of the samples as compared to the gas phase treated samples. Liquid phase treatment has improved the order of the graphitic character of the carbon wall.

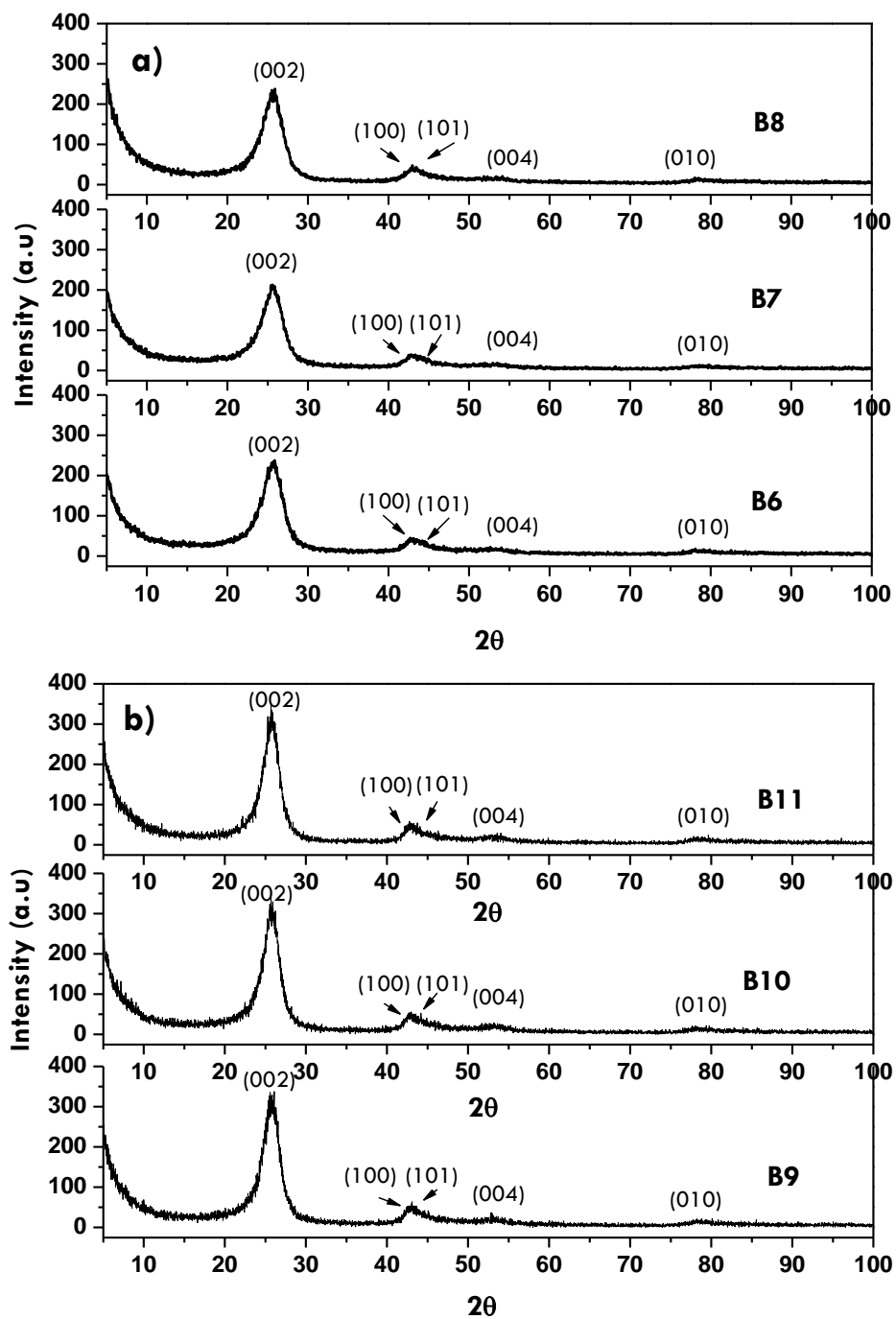


Figure 4.12: X-ray diffraction patterns of (a) gas phase (b) liquid phase functionalized samples.

4.6 Raman spectroscopy

Raman spectra of the functionalized samples and the quantitative results are summarized in Figure 4.13 and Table 4.2. Raman spectra of functionalized samples contain two domains in the range of 1000 – 1800 cm^{-1} . The first one located at $\sim 1340 \text{ cm}^{-1}$ is denoted as D band, as it is related to scattering from disordered carbon and amorphous carbon impurities present in the MWCNTs samples. The disordered carbon structure is due to the finite or nanosized graphitic planes and other forms of carbon, such as rings along with defects on the nanotube walls, vacancies, heptagon-pentagon pairs, kinks and heteroatoms (Datsyuk et al., 2008). The second feature with an approximate frequency range of 1550 to 1600 cm^{-1} is referred to as the graphite (G) band. In graphite, the G band exhibits a single peak at 1582 cm^{-1} related to tangential mode vibration of the carbon atoms (Haris, 2009 ; Jorio et al., 2003).

Table 4.2: The Raman shift (cm^{-1}) and the I_D/I_G ratio for functionalized MWCNTs samples

Treatment	Raman shift (cm^{-1})		I_D/I_G
	D	G	
B6	1327.94	1598.05	1.51
B7	1328.74	1601.81	1.59
B8	1327.15	1601.06	1.53
B9	1347.74	1571.43	1.17
B10	1347.27	1585.06	1.18
B11	1343.98	1564.85	1.16

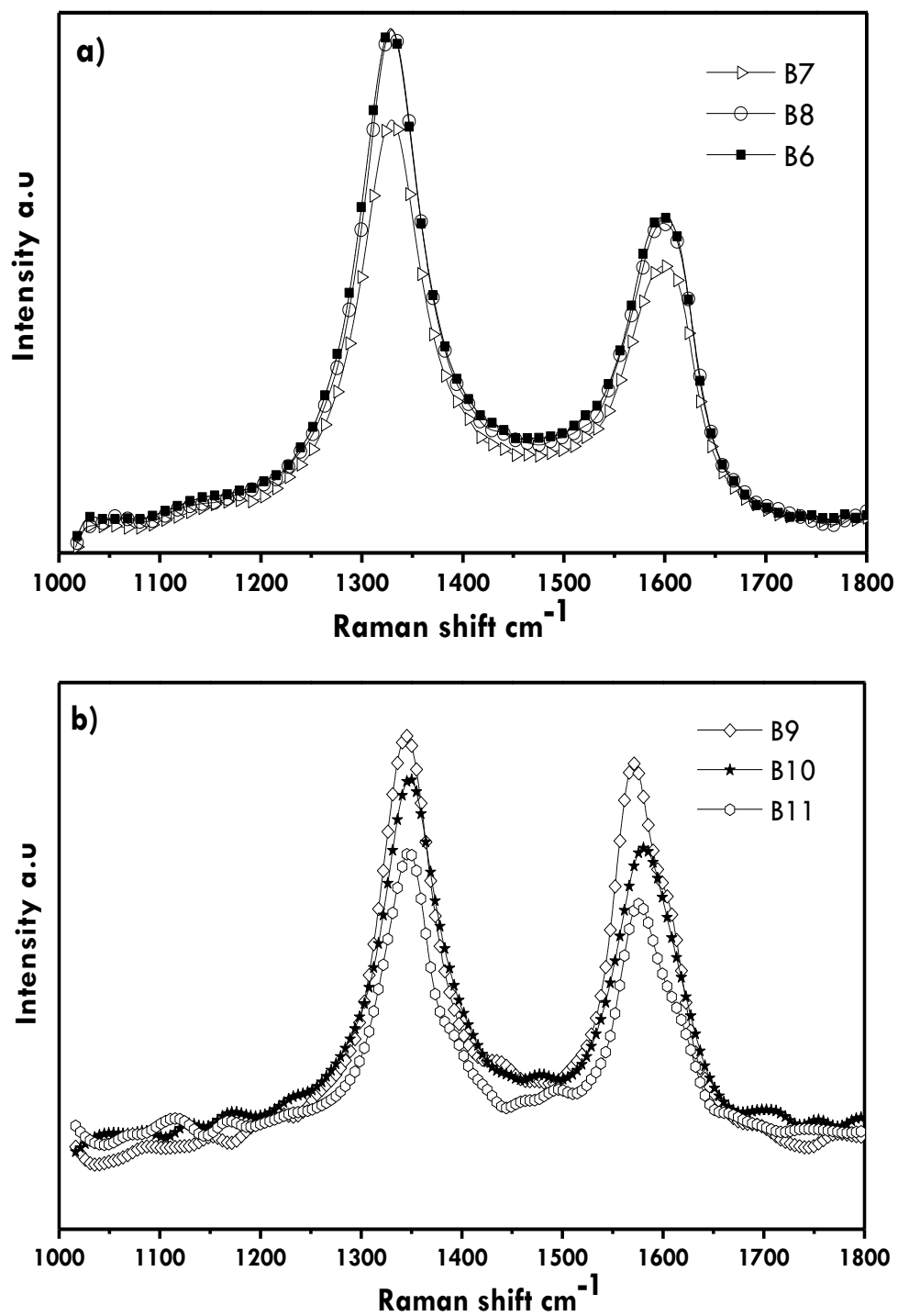


Figure 4.13: Raman scattering spectra of (a) gas phase (b) liquid phase functionalized samples

The degree of functionalization was quantified using the D to G band intensity ratio (I_D/I_G) ratio which is the intensity of the disorder mode at 1360 cm^{-1} divided by the intensity of graphite mode at 1600 cm^{-1} . In this study, the I_D/I_G ratio is shown in Table 4.2 with values of 1.51, 1.59, 1.53, 1.17, 1.18, 1.16 for samples B6, B7, B8, B9, B10, and B11, respectively. The gas phase samples showed the highest number of I_D/I_G ratio compared to the liquid phase samples. For instance, B7 showed the highest number of I_D/I_G value of 1.59 as compared B11 value of 1.16. Generally, an increase in the I_D/I_G ratio indicates an increase in the number of defects on the sidewall of the MWCNTs (Jeong et al., 2010). Thus, it can be concluded that the gas phase treatment has created high degree of defect on the sidewall of MWCNTs as compared to liquid phase treatment. This is in good agreement with the titration result where the gas phase exhibits the highest numbers of acidic functional groups anchored onto MWCNTs.

Also, it is interesting to note that the band frequency for all samples show noticeable shifts in certain characteristic vibrational modes. Gas phase functionalized (B6, B7 and B8) samples show the shifted D and G band frequency of upshift and downshift of about 1 to 3 cm^{-1} . The B6 and B8 samples have almost the same D band frequency of about 1327.94 and 1327.15 cm^{-1} respectively. The D band frequency for B7 is 1328.74 cm^{-1} . The sample B7 shows slight upshift of D band frequency as compared to B6 and B8. For the liquid phase functionalized samples, the D band frequency for B9 and B10 are almost the same at 1347.74 and 1347.27 cm^{-1} , respectively. While, for the B11 sample D band frequency downshift of about 3 cm^{-1} was observed. On other hand, the B9, B10, and B11 samples show significant G band frequency shift between each other of about 7 to 21 cm^{-1} with the band frequency of 1571.43 , 1585.06 and 1564.85 cm^{-1} , respectively. The shifting of the D band frequency

might be due to the chemical charge transfer of the functionalized samples at different temperature treatment (Dresselhaus et al., 2004). The introduction of bulky sulfur containing functional groups on the surface of CNTs induces strain on the nanotubes walls and thereby results in the shifting of the peaks. This explains why the B7 and B11 showed greater shift than the other samples. These result was consistent with the TGMS analysis where the evolution of SO and SO₂ gasses was observed from both gas and liquid phase treatment. In addition, these results are also in good agreement with titration data where B7 has the highest acidic functional group and B11 has the lowest acidic functional groups. In addition, the G band frequencies for all samples also show the same features of upshifting and downshift of peaks.

As reported by Wise and colleagues, the removing of charge from CNTs walls such as oxidation process resulted in an upshift in the G band peak, while adding charge to CNTs walls, for example reduction, resulted in a downshift. The downshift observed upon is easily understood: as the additional electron density is placed in the anti bonding conduction bands of the CNTs, the average C–C bond strength is weakened, resulting in a downshift or softening of the vibrational frequency. The reason for the upshift that occurs is less obvious. One would intuitively expect that removing electron density from the fully occupied, bonding valence band of a SWCNTs would weaken the C–C bonding, resulting in a downshift in the G band frequency. Functionalization causes a local change in the hybridization from sp² to sp³ of the sidewalls carbon atom. One possible explanation for the upshift to occur might be due to the addition of some sp³ character to sp² hybridized orbitals which results from the curvature of the graphitic structure required to form a tube, results in Coulomb repulsion, particularly in small

diameter tubes. Removing electron density from these orbital reduces the repulsion, resulting in stronger net bonding and a higher G band frequency (Wise et al., 2004).

4.7 Texture and porosity of the functionalized MWCNTs

The textural properties of the gas and liquid phase functionalized samples are summarized in Table 4.3. Generally, all functionalized samples exhibit a high mesoporous volume as compared to microporous and macroporous surface properties. As referred to the N₂ adsorption-desorption isotherms, the BET surface area for gas phase treated sample, B6, B7 and B8 are 332.76, 304.68 and 316.03 m²/g, respectively, see Figure 4.14 (a). From the isotherm, region at 0 to 0.3 of P/P₀ indicates the presence of microporous with small volume. There is no significant steep rise in the isotherm at partial pressure < 0.3 P/P₀, indicating very low micropore density in all three samples of gas phase treatment. Regions above 0.3 of P/P₀ indicates the features of the Type IV isotherm with a clear hysteresis loop and plateau at high P/P₀. The type IV isotherm is the characteristic of H1 hysteresis loop that is due to the capillary condensation of the gas in mesopores, and limiting uptake over a range of high P/P₀. These type of isotherm are given by mesoporous adsorbent materials (Sing, 1982).

Table 4.3: Textural properties of functionalized MWCNTs samples

Samples	Treatment temp (°C)	BET Surface area (m ² /g)	Micropore volume (cm ³ /g)	Total pore volume (cm ³ /g)	Mesopore volume (cm ³ /g)
B6	100	332.76	0.2486	1.586	1.3374
B7	200	304.68	0.2285	1.444	1.2155
B8	300	316.03	0.2433	1.508	1.2647
B9	100	206.50	0.1693	0.5204	0.3511
B10	200	245.90	0.2035	0.8700	0.6665
B11	300	256.60	0.1744	0.6823	0.5079

The N₂ adsorption-desorption isotherm of liquid phase samples are presented in Figure 4.14(b). The BET surface area for liquid phase samples show lower values than gas phase samples. For B9, B10 and B11 the BET surface areas are 206.50, 245.90, and 256.60 m²/g, respectively. These samples also show the presence of small volume of micropore as the region of isotherm from 0 to 0.3 P/P_o is no significant steep rise. As the region more than 0.3 P/P_o , the isotherm graph exhibit the same condition as gas phase treated samples.

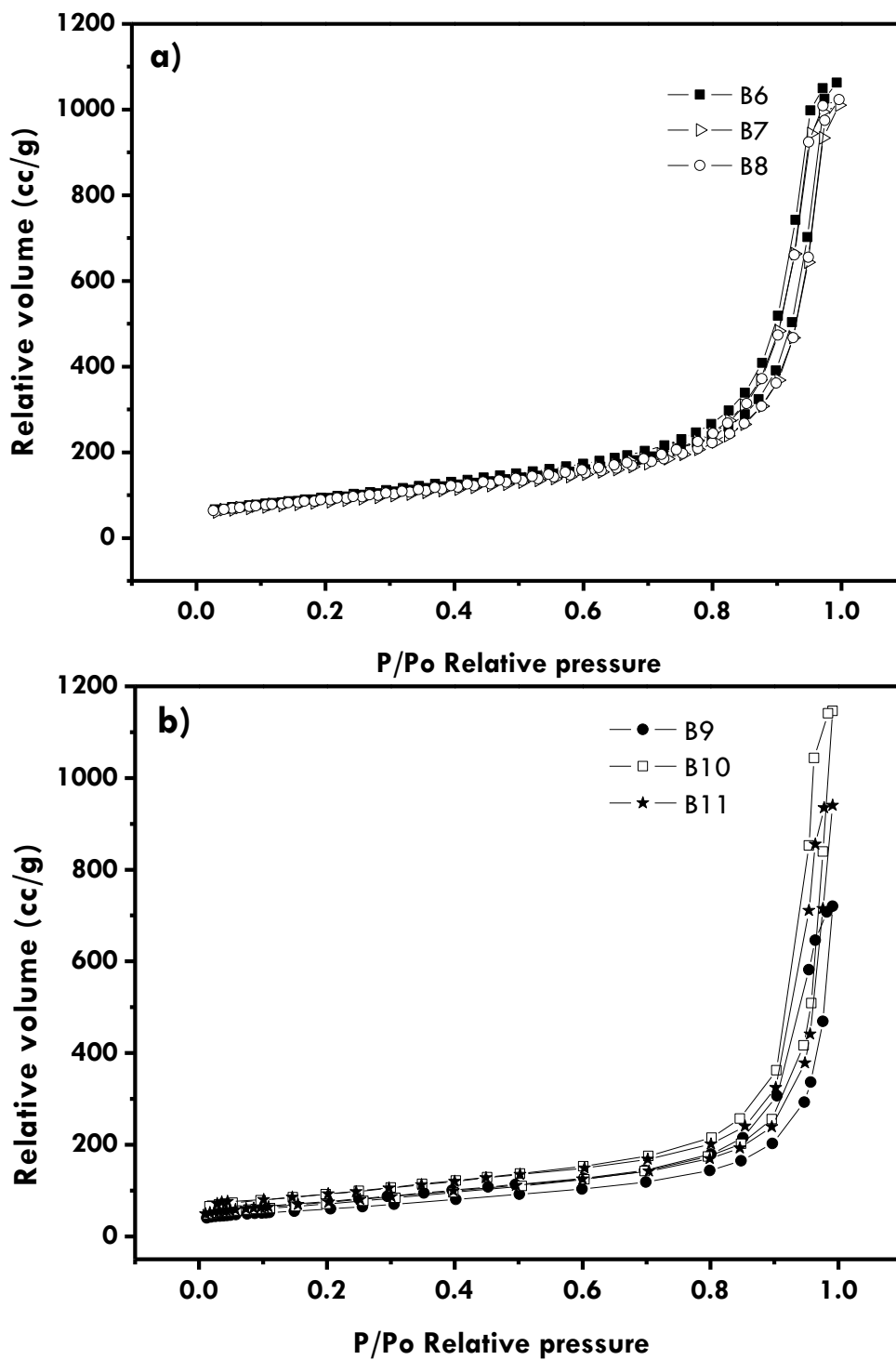


Figure 4.14: Nitrogen adsorption-desorption isotherms of (a) gas phase (b) liquid phase functionalized samples.

Figure 4.15(a) and(b) shows the pore size distributions of gas and liquid phase samples from experimental isotherm using the Kelvin model of pore filling of Barrett, Joyner and Halenda (BJH) method. This method only applies to the mesoporous and small macroporous size range. The pores can be classified according to their sizes:

- (i) Pores with widths exceeding about 50 nm (0.05 μ m) are called macropores;
- (ii) Pores of widths between 2 nm and 50 nm are called mesopores;
- (iii) Pores with widths not exceeding about 2 nm are called micropore.

The BJH method for gas phase shows the continuous distribution with two different pore modes of width between 2 and 5 nm in diameter, see Figure 4.15 (a). This indicates properties of the smaller mesopores. While pore of width of 6 to 130 nm in diameter indicates the large pore surface properties. The pore size distribution shows the characteristic of mesoporous surface with the size between 2 to 50 nm (20 -500 Å). The similar pattern of size distribution has been reported by Tessonier and co-workers. They suggested that the small pores corresponded to the inner channel of the nanotubes, while the larger pores were formed between the entangled nanotubes (Tessonier et al., 2009).

As shown in Figure 4.15 (a), the B7 and B8 have similar size distribution and the contribution of pores greater than 50 nm is lower than B6, tend to indicate that the B7 and B8 were less entangled. The pore diameter region of 2 to 5 nm, samples B6, B7 and B8 show slightly the same reduces of the pore volume with the characteristic peak with a maximum around 2.5 nm. In contrast, in pore diameter region of 5 to 60 nm, B7 and B8 show the same values of pore volume but B6 shows slightly high in the magnitude of pore volume with the characteristic peak that is at maximum around 25 nm. This

indicates the B6 samples possess slightly higher cumulative pore volume as compared to B7 and B8.

The BJH method of pore size distribution for liquid phase samples shows also continuous distribution of two different modes of width 2 to 5 nm and 60 to 100 nm in diameter, see Figure 4.15(b). In the pore size region of 2 to 5 nm, the B11 shows slightly high magnitude of pore volume with the characteristic peak that is maximum around 2.5 nm as compared to B10 and B11. This indicates that B11 has slightly higher small mesopores. In the pore size at the region of 60 to 100 nm, B9 shows slightly lower magnitude of pore volume than B10 and B11. This indicates that B9 has slightly low in large pore of mesoporous. At this region, the liquid phase samples show the lower magnitude of pore volume as compared to gas phase samples. This is due to the high large pore of mesoporous in the gas phase sample.

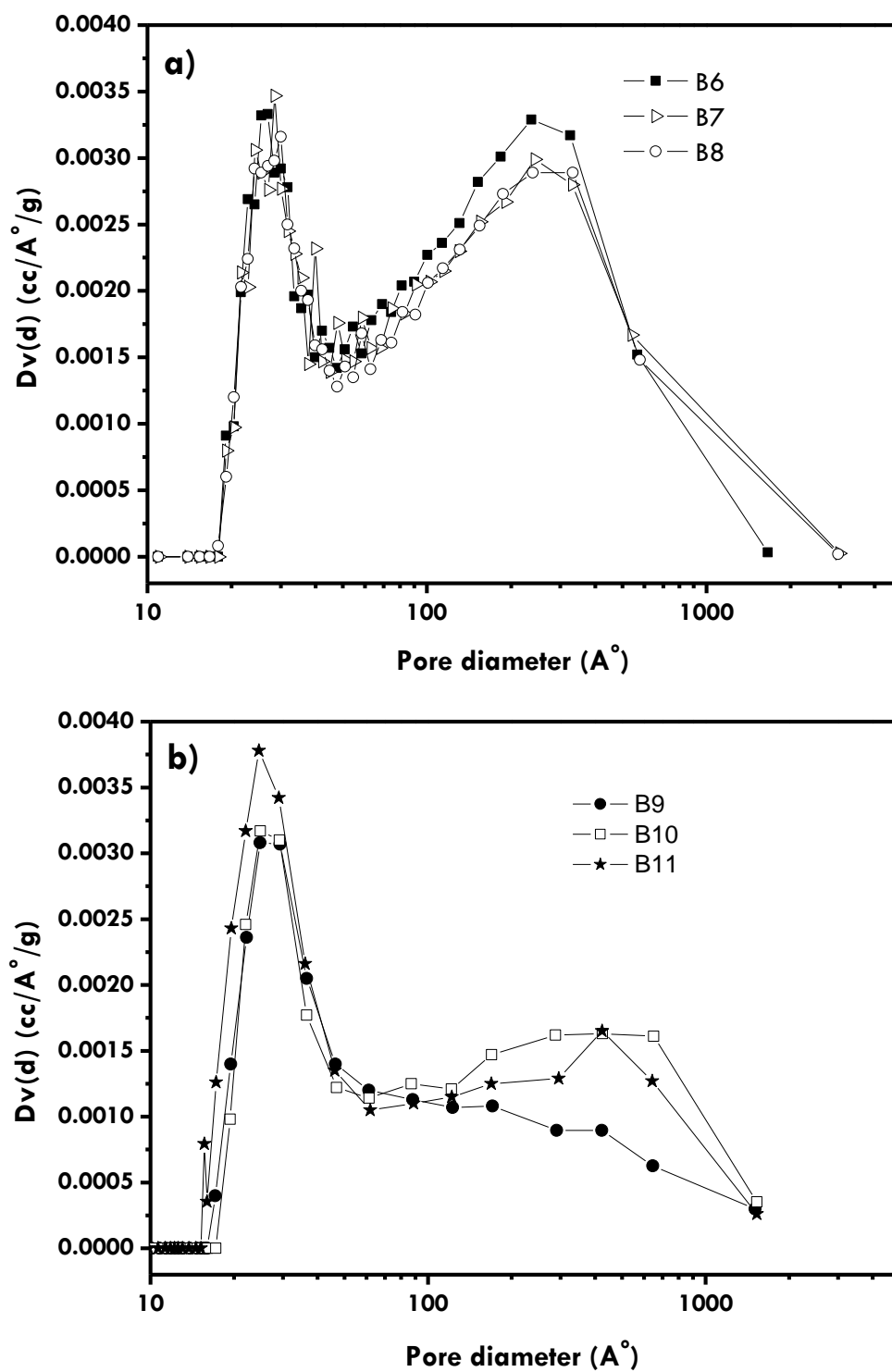


Figure 4.15 : Pore size distribution of (a) gas phase (b) liquid phase functionalized samples.

4.8 High Resolution Transmission Electron Microscopy (HRTEM).

Transmission electron microscopy (TEM) is an important technique for characterizing nanostructured materials as it provides information on the morphology of nanostructures. For the CNTs, it provides their microstructural properties such as the orientation of the walls, graphitic character and the presence of carbon and metal impurities on the carbon surfaces. The representative TEM images of gas phase treated samples are shown in Figures 4.16, 4.17 and 4.18, respectively. The representative TEM images of liquid phase treated samples are shown in Figures 4.19, 4.20 and 4.21, respectively.

Figure 4.16 shows TEM images of the B6 sample, that was sulfonated at 100 °C. Figure 4.16 (a) shows the tubes were loosely packed and stretched out from each other. Furthermore, the curled tubes were observed in this sample, see Figure 4.16 (b) and 4.16 (c), which caused by agglomeration of MWCNTs. These curled tubes might be due to the lesser oxidation process occurred onto the MWCNTs surfaces due to the low temperature (100 °C) of acid treatment. The low treatment temperature might not be enough to destroy relevant bonds located on the MWCNTs surfaces.

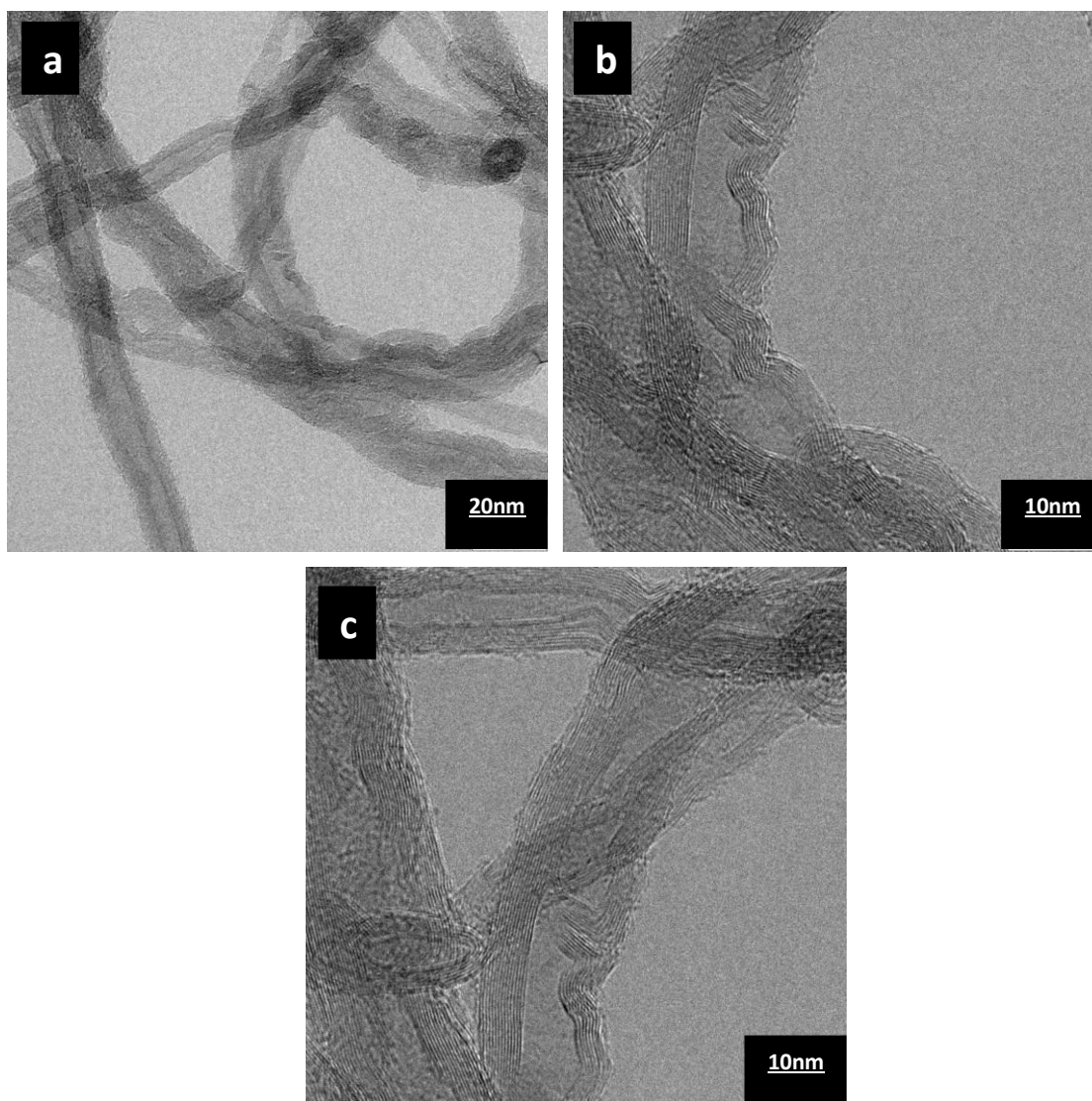


Figure 4.16: The TEM images of gas phase treated sample at 100 °C (B6) are shown above. The loosely packed and show very little amorphous carbon on the surface. Also visible are surface defects.

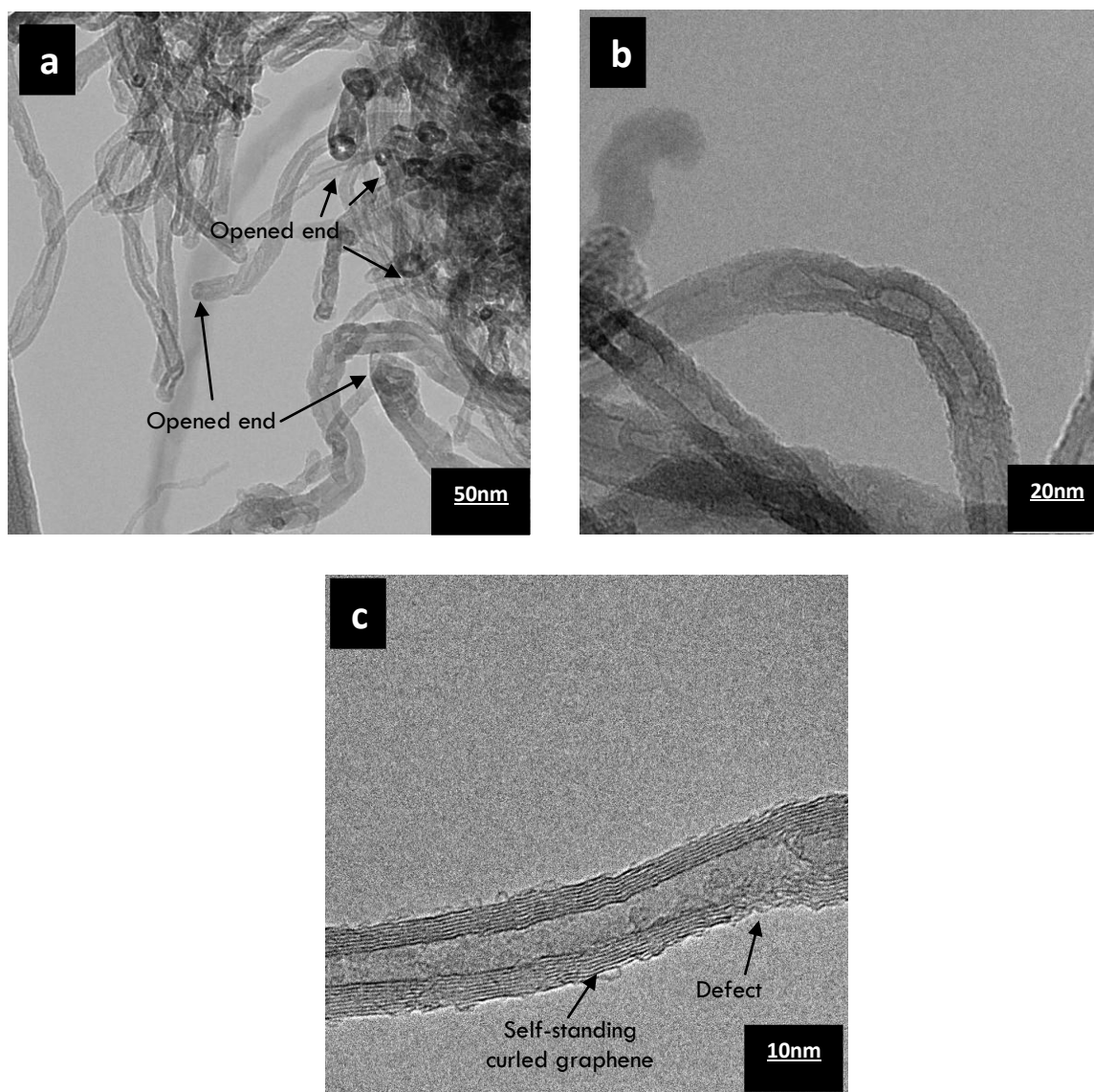


Figure 4.17: The TEM images of gas phase treated sample at 200 °C (B7) are shown above. The overview of open-ended MWCNTs caps .The defective region of B7 samples.

Figure 4.17 shows the TEM images of B7 sample that was sulfonated at 200 °C. As shown in Figure 4.17 (a), open ends of MWCNTs were observed. The cap of the MWCNTs was removed by purification process at the pre-treatment stage. Also, the sulfonation process at 200 °C might effect more opening of the MWCNTs ends. The hollow ring patterns were observed since the caps of B7 sample were open.

As shown in Figure 4.17 (c), 4.19 (b) and 4.20 (c), the presence of physical defective region on the outer wall of MWCNTs surfaces. Besides, these samples shows small amount of debris-like highly disordered carbon and self-standing curled graphene sheet on the outermost surface of carbon. As shown in Figure 4.16 (a), 4.17 (a), 4.18, 4.19 (a), 4.20 (b), and 4.21 (a) all gas and liquid samples exhibit the same narrow tubular morphology.

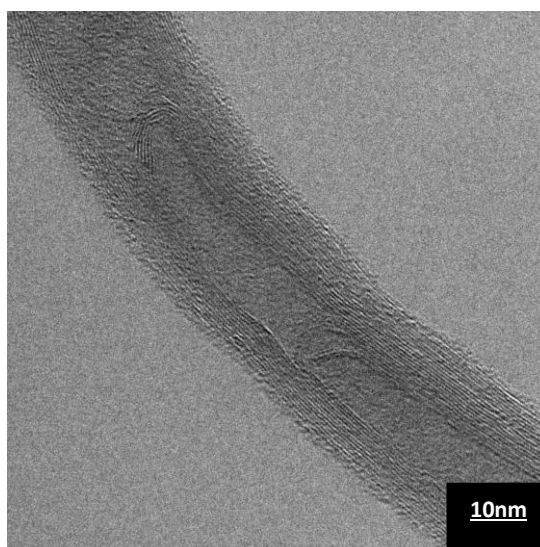


Figure 4.18: The TEM image of gas phase treated sample at 300 °C (B8) is shown above.

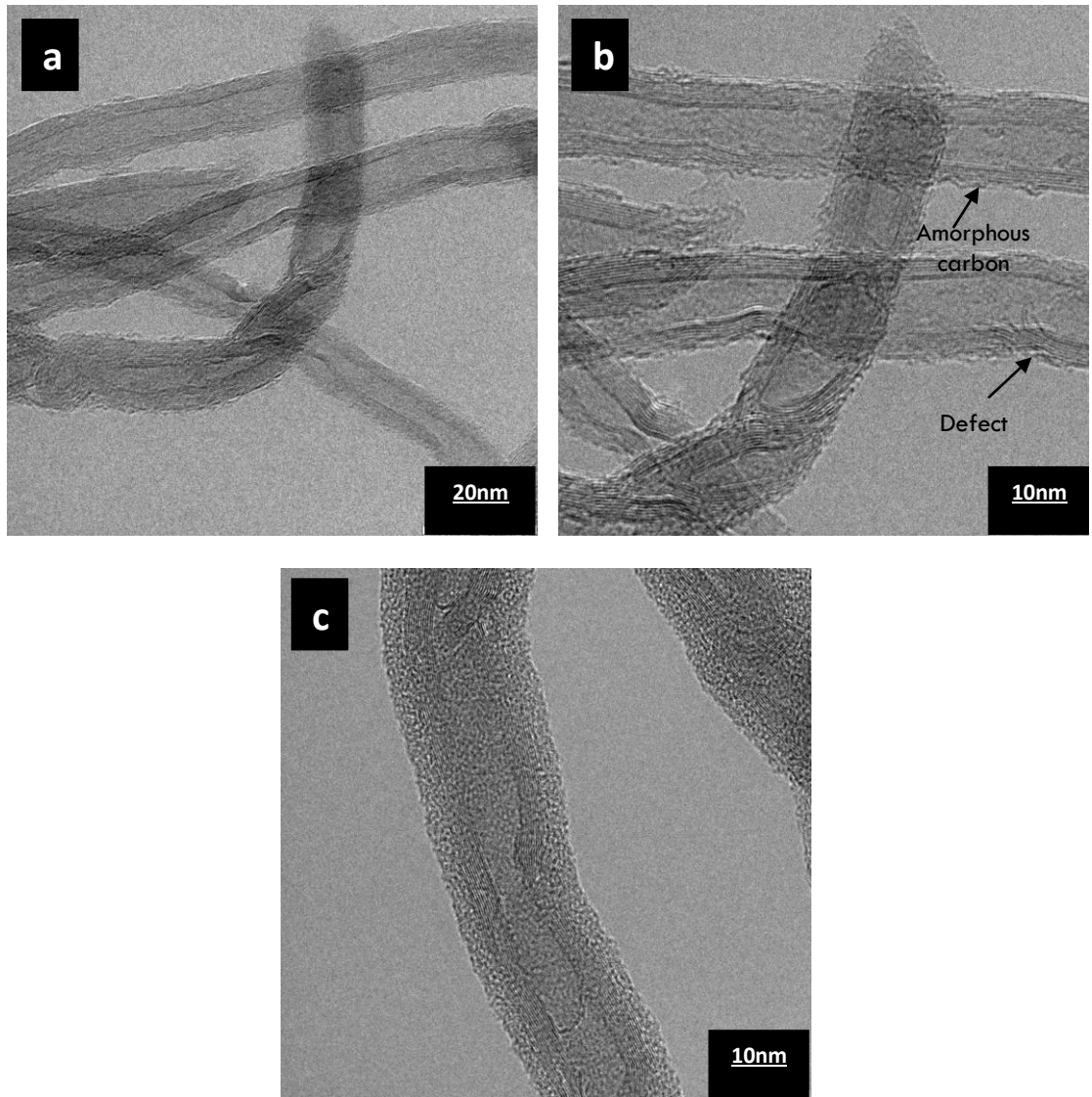


Figure 4.19: The TEM images of liquid phase treated sample at 100 °C (B9) are shown above. Physical defective region on the outer wall of MWCNTs surfaces and debris-like highly disordered carbon.

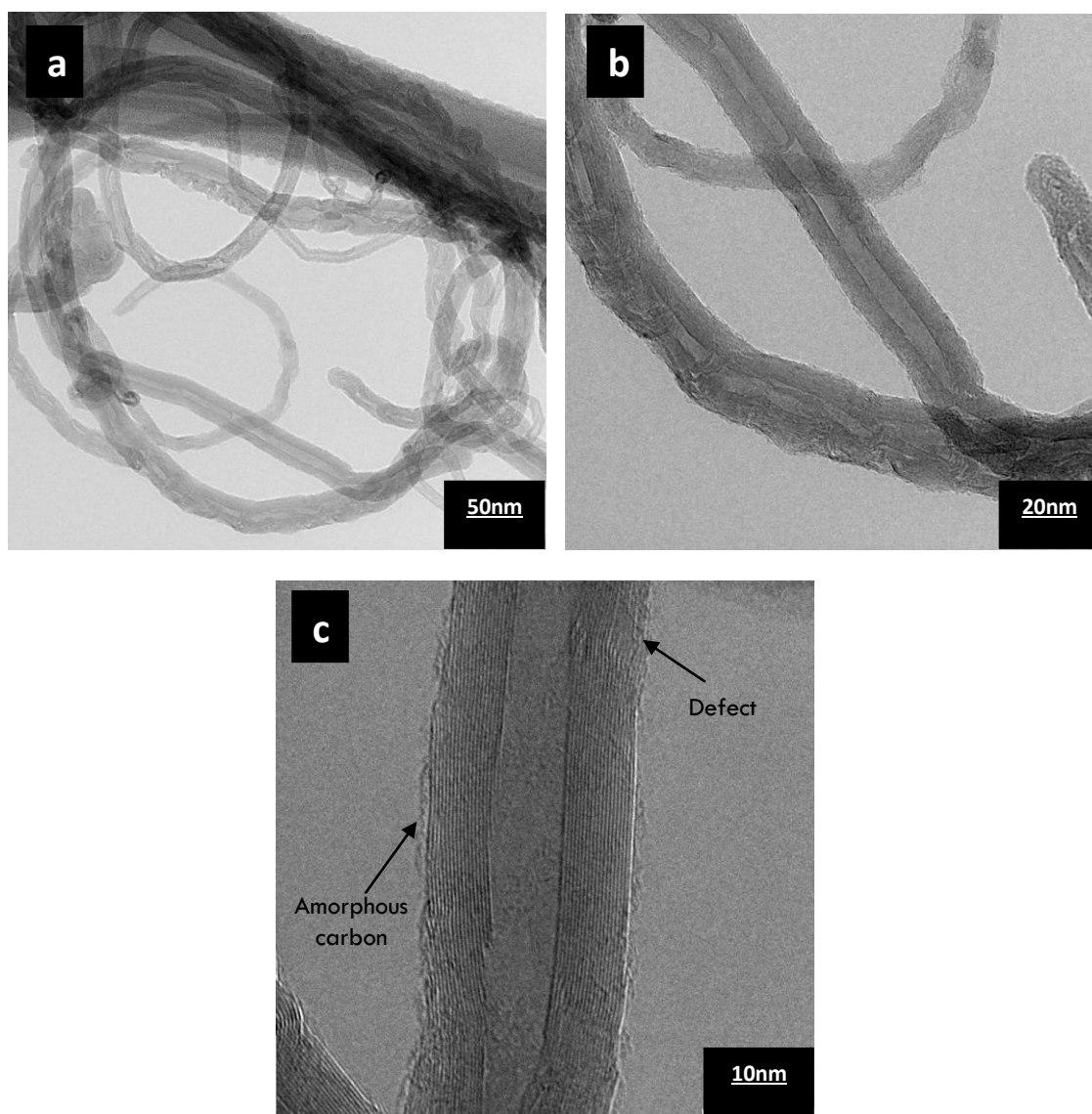


Figure 4.20: The TEM images of liquid phase treated sample at 200 °C (B10) are shown above. Narrow tubular morphology of MWCNTs is shown. Physical defective region on the outer wall of MWCNTs surfaces.

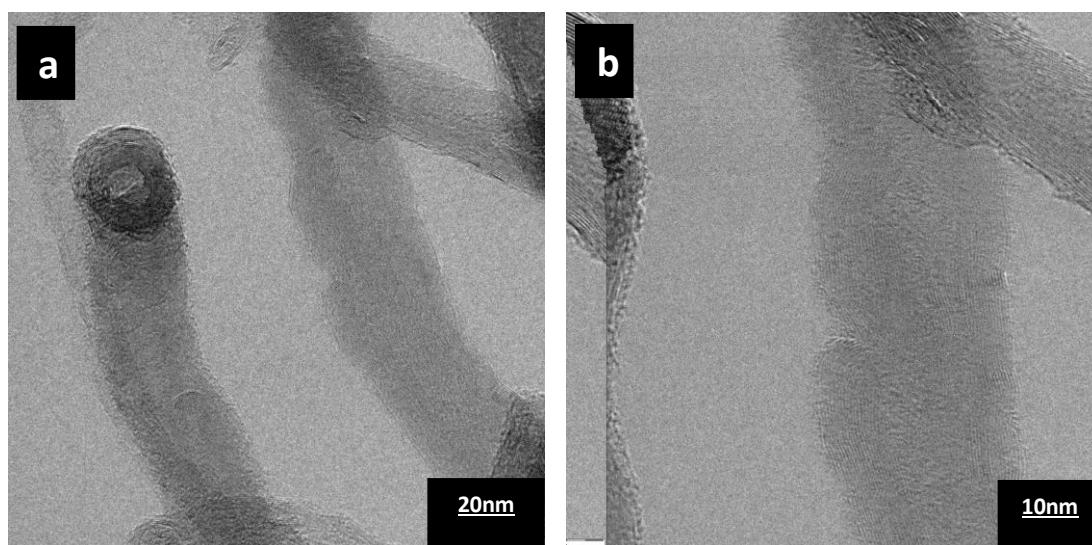


Figure 4.21: The TEM images of liquid phase treated sample at 300 °C (B11) are shown above.

4.9 Equilibrium Adsorption of Mercury Ion on Adsorbents

The analytical performance of three different adsorbents including pristine, B7 (gas phase) and B10 (liquid phase) was tested for a series of initial mercury ion concentration. The equilibrium study was conducted by varying the mercury concentration from 20 to 600 mg/L at pH 6, 0.3 g of adsorbent dosage, 180 rpm agitation speed for 6 hours. The pH of the mercury aqueous solution was selected at pH 6 on the basis of many researchers report that at pH ranging from 4 to 7 the optimum removal was achieved for most of metals tested (Tawabini et al., 2010; Atieh et al., 2010; Zhu et al., 2009). For example, at low pH values below 2, the hydrogen ions (H^+) are likely to compete with mercuric ion (Hg^{2+}) and at pH values above 6.5 mercuric ions might precipitate (Mohan et al., 2001)

The adsorption capacity, Q_e , (mg/g) of mercury on pristine, B7 and B10 at an initial mercury concentration range of 20 to 600 mg/L are shown in Figure 4.22. As

shown in Figure 4.22, the adsorption capacity of mercury onto MWCNTs was improved significantly after functionalization. The results showed that an initial rapid uptake of mercury ions was observed within the concentration of 20 to 300 mg.L⁻¹ for pristine and B7 adsorbents. The adsorption capacity of mercury is only 58.76 mg/g for the pristine at almost equilibrium concentration of 300 mg.L⁻¹ while the adsorption capacity increases and reaches 80.37 mg/g for B7 sample at the same equilibrium concentration of mercury. The mercury uptake slowly increases from 400 mg.L⁻¹ to 600 mg.L⁻¹ and almost reached equilibrium for both pristine and B7 adsorbent. In contrast, the B10 adsorbent showed an initial rapid mercury uptake within the concentration of 20 to 400 mg.L⁻¹ until the equilibrium was reached at 500 mg.L⁻¹ (Figure 4.22).

Pristine samples exhibit the lowest value of mercury uptake of 62.98 mg/g at 600 mg.L⁻¹ mercury concentration followed by B7 value of 94.67 and B10 value of 123.98 mg/g. The B10 exhibits the highest removal of mercury as compared to pristine and B7 samples. The high sorption capacity by B10 and B7 suggested a high affinity of the surface acid functional groups on the MWCNTs surfaces to the mercury ions. The uptake efficiency of mercury ion was observed to be dependent on the initial mercury concentration where the mercury uptake rapidly increases at low mercury concentration until equilibrium is reached at high mercury concentration. At low concentration of 20 to 300 mg/L the plot was linear. It is postulated that a change in the adsorption mechanism occurs with the increase in the mercury concentration up to 600 mg.L⁻¹.

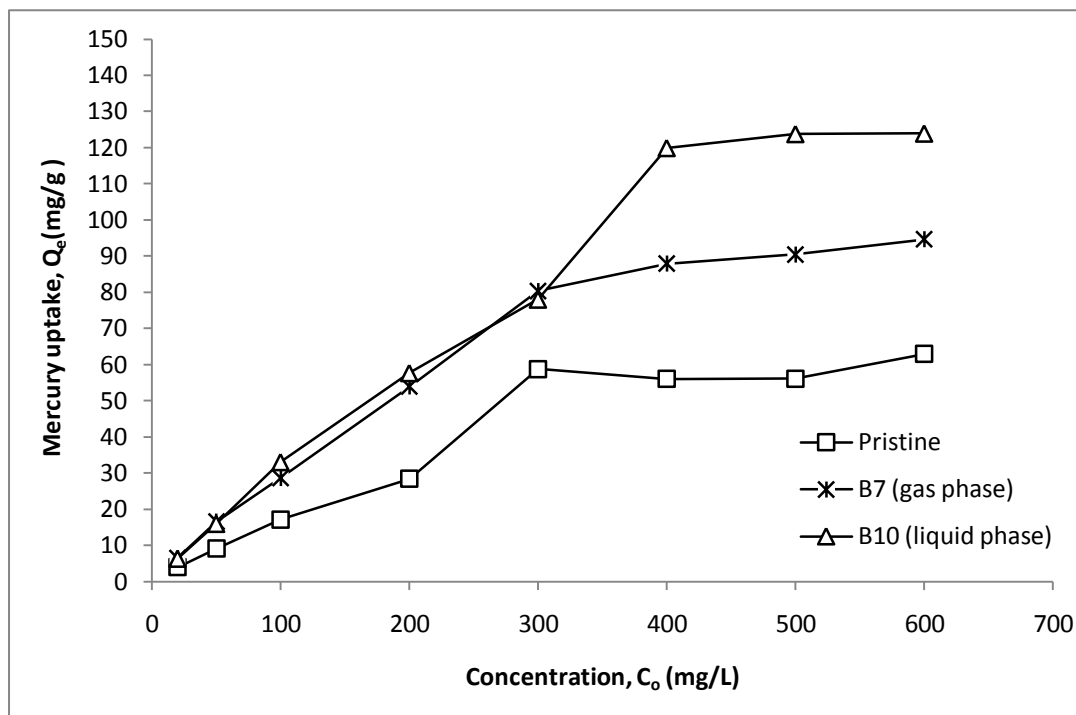


Figure 4.22: The effect of initial concentration on the adsorption of mercury (II) ions by Pristine, B7 (gas phase) and B10 (liquid phase) adsorbent. [Conditions; adsorbent dose: 0.3000g; pH: 6; contact time: 6 hours; temperature: 25 °C; agitation rate = 180 rpm]

As the result shows, B10 adsorbent has higher adsorbability for the adsorption of mercury ion as compared to B7 adsorbent sample. This is inspite of the fact that the B7 adsorbent exhibits the excellent characteristic such as highest acidic functional groups (see Table 4.1), greatest specific surface area (see Table 4.3) and high mesopores distribution (see Figure 4.15) than B10 adsorbent sample. Two postulates is proposed to explain the highest adsorption capacity achieved by B10 adsorbent sample. The first postulate, the oxidation of B10 using HNO_3 and H_2SO_4 by liquid phase treatment tends to increase oxygen functional groups such as hydroxyl group (O – H) on B10 adsorbent surface. As observed from IR result, the presence of strong broad unbounded hydrogen (free hydroxyl, OH:OH) group and hydroxyl group (O-H) on the B10 adsorbent surfaces helps the B10 adsorbent become better hydrophilic which in turn promotes the formation of water cluster on B10 adsorbent surface. In contrast, the presence of sulphur

functional (sulfonates ester) group such as R-SO₂O⁻ and other sulphur (C – S and S – O – C) on B7 adsorbent introduced by mixture of H₂SO₄/SO₃ (Oleum) using the gas phase reaction does not have a strong affinity interaction as hydroxyl groups (O – H) in aqueous solution. Therefore, the B7 adsorbent could not disperse well in the aqueous mercury solution. As a result, the less interaction between mercury ion and the acidic functional group on the B7 surface was considered. Thus, the B10 adsorbent has better interaction in aqueous mercury solution than B7 adsorbent sample. The second postulate is the sulphur group might be less stable in the aqueous solution. Thus, the sulphur groups tend to detach or leach out from the B7 surface during the agitation step in the adsorption experiment. The sorption isotherm models was established to determined the maximum sorption capacity and the adsorption favourable of the three different adsorbent (Pristine, B7 and B10) for mercury ion using Langmuir and Freundlich isotherms.

4.10 Langmuir and Freundlich Isotherms

The equilibrium adsorption data of mercury for three different adsorbent (pristine MWCNT, B7 and B10) were analyzed according to the Langmuir and Freundlich isotherm models. These isotherm models have been widely used by many researchers (Namasivayam & Kadirvelu, 1999; Zhu et al., 2009; Okeola & Odibunmi , 2010; Shadbad et al., 2011). The linear equations of these models are expressed by the equations below:

$$\frac{C_e}{Q_e} = \frac{1}{q_m K_a} + \frac{C_e}{q_m} \quad \text{----- Langmuir} \quad (4)$$

$$\log(Q_e) = \frac{1}{n} \log(C_e) + \log(K_F) \quad \text{----- Freundlich} \quad (5)$$

The adsorption isotherm designates how the adsorbed molecules allocate between the liquid phase and the solid phase when the adsorption process reaches an equilibrium state. Langmuir and Freundlich isotherm were used in adsorption study to explain the phenomena and understand the degree of favourability and extent of adsorption process (Okeola & Odibunmi, 2010).

For the calculation of each isotherm constant, initial concentration of mercury was varied (20, 50, 100, 200, 300, 400, 500 and 600 mg/L) for sorption by the constant weight of each adsorbents of 0.3g for sorbate sorbent contact time of 6 hours at 180 rpm. The parameters of the Langmuir and Freundlich isotherm models, q_m , K_a , K_F and n which are the adsorption capacity, the adsorption affinity, the sorption capacity and degree of adsorption favourable, respectively. These parameters and the correlation coefficient of determination, R^2 , (Namasivayam & Kadirvelu, 1999; Hawaiah et al., 2004; Zhu et al., 2009; Yavari et al., 2011) are summarized in Table 4.4 as determined from the linear regression analysis of experimental data. The correlation coefficient (R^2) values obtained from both isotherm models were a measure of goodness-of-fit of the isotherm models to the adsorption behaviour of mercury ion onto the three (Pristine, B7 and B10) different adsorbent. From the slope and intercepts of Langmuir isotherm, the maximum sorption capacity (q_m) of mercury was calculated. In the Freundlich isotherm, n value between 1 and 10 represents a favourable adsorption of the metal ion onto adsorbent (Zhu et al., 2009). The high value of n indicates a strong bond between the adsorbent and the adsorbate. The values of Freundlich constant, K_F in the linear plot indicates the extent of metal ion removal hence a measure of adsorption capacity as Langmuir model (q_m) (Okeola & Odebunmi, 2010).

The Langmuir isotherm model assumed that adsorption takes place only at specific localized sites on the surface and the saturation coverage corresponds to complete occupancy of these sites. Each site can accommodate only one molecule or atom. There is no interaction between the neighbouring adsorbate molecules or atoms and localized monolayer adsorption on a homogeneous surface (Czepirski et al., 2000; Yavari et al., 2011). The Freundlich model is an empirical relationship describing the adsorption of solutes from a liquid to a solid surface, and assumed that different sites with several adsorption energies are involved (Chen et al., 2004; Yavari et al., 2011).

Table 4.4: Langmuir and Freundlich isotherm parameters for adsorption of mercury (II) ion onto pristine MWCNTs, B7 and B10 samples.

Samples	Langmuir Isotherm				Freundlich Isotherm		
	q_m (mg/g)	K_a (L/mg)	R_L	R^2	K_F	n	R^2
Raw MWCNTs	92.52	0.00536	0.9032	0.8761	-0.0084	1.3710	0.9388
B7	98.04	0.0596	0.4561	0.9907	1.1585	2.8310	0.9238
B10	135.04	0.0477	0.5118	0.9616	1.2385	2.5673	0.7465

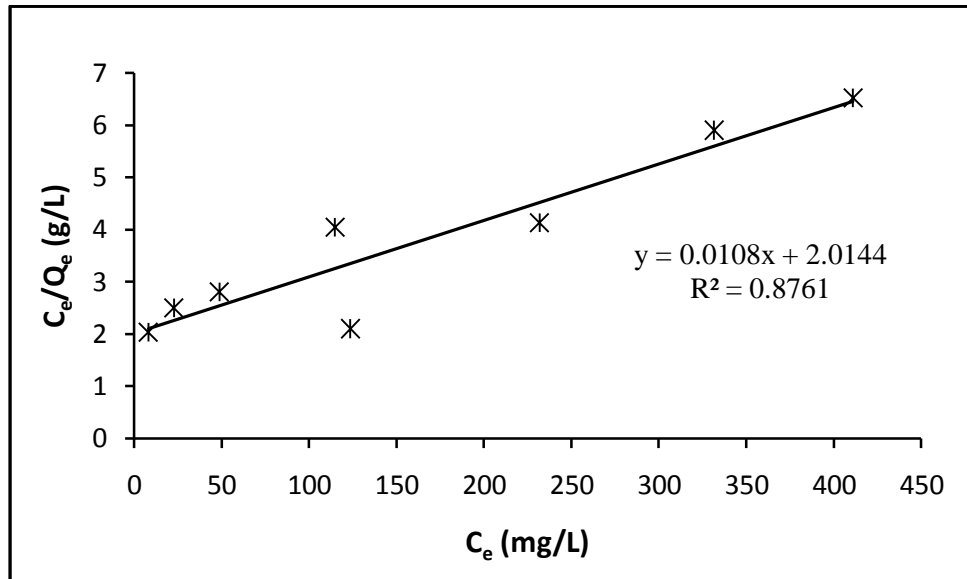


Figure 4.23: Linear plot of Langmuir Isotherm for pristine MWCNTs sample. [Conditions; adsorbent dose: 0.3000g; pH: 6; contact time: 6 hours; temperature: 25 °C; agitation rate = 180 rpm]

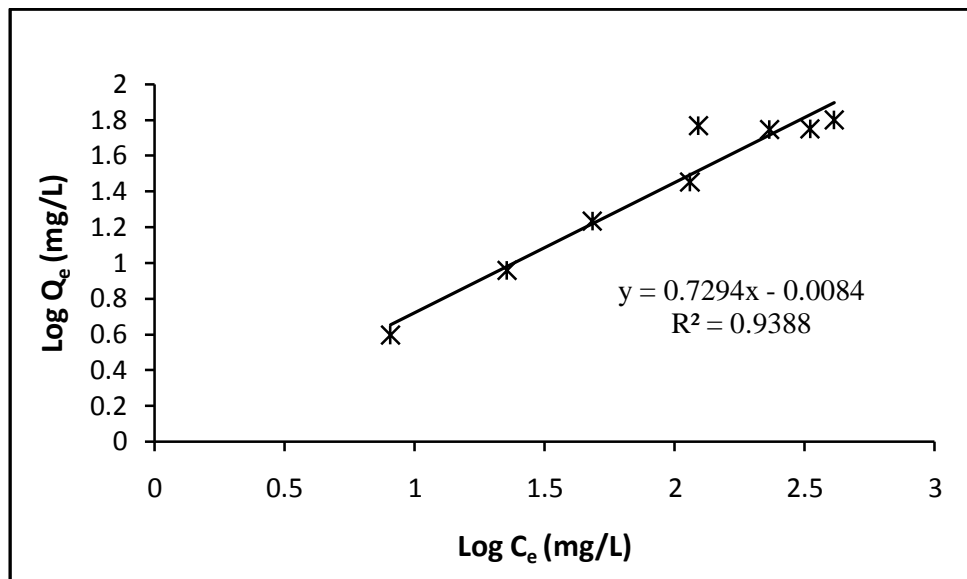


Figure 4.24: Linear plot of Freundlich Isotherm for pristine MWCNTs sample. [Conditions; adsorbent dose: 0.3000g; pH: 6; contact time: 6 hours; temperature: 25 °C; agitation rate = 180 rpm]

The linear plot of a specific sorption (C_e/Q_e) against the equilibrium concentration (C_e) shows that, the adsorption from series of mercury ion concentration for pristine MWCNTs fit the Langmuir poorly with the coefficient (R^2) of 0.8761, see Figure 4.23. This poor Langmuir fitting gave the maximum sorption capacity (q_m) of 92.52 mg/g. As shown in Table 4.4, the constant R_L value of 0.9032 ($0 < R_L < 1$ is favourable) which indicates that the favourable adsorption of mercury ion onto pristine. But the R_L value (0.9032) seem closed to 1 ($R_L = 1$ is linear) which might be a linear adsorption characteristic. The poor fit to Langmuir isotherm might suggest that incomplete monolayer coverage of mercury ion on pristine surface.

In contrast, the linear plot logarithm sorption ($\log Q_e$) against logarithm equilibrium concentration ($\log C_e$) of adsorption data obtained experimentally from the series mercury concentration for pristine fitted well to the Freundlich isotherms with the correlation coefficient (R^2) of 0.9388, see Figure 4.24. The Freundlich constant, K_F gave the negative value ($K_F = -0.0084$ mg/g) indicating that there was no extent of mercury removal from pristine. The two Langmuir and Freundlich constants K_a and n of pristine have a low value of 0.00536 and 1.3710 respectively, as compared to B7 and B10 adsorbent samples. The low value of n constant indicates the weak bond between the adsorbent and the adsorbate (mercury ion) (Okeola & Odebunmi, 2010). The well fitted Freundlich model might be due to the adsorption of mercury ion onto heterogeneous solid surface of pristine. This heterogeneous surface of pristine was related to the presence of amorphous carbon and trace metal catalyst impurities on the pristine surface. This interaction is assumed to have weak binding side between mercury ion and heterogeneous pristine surface because the low value of n constant.

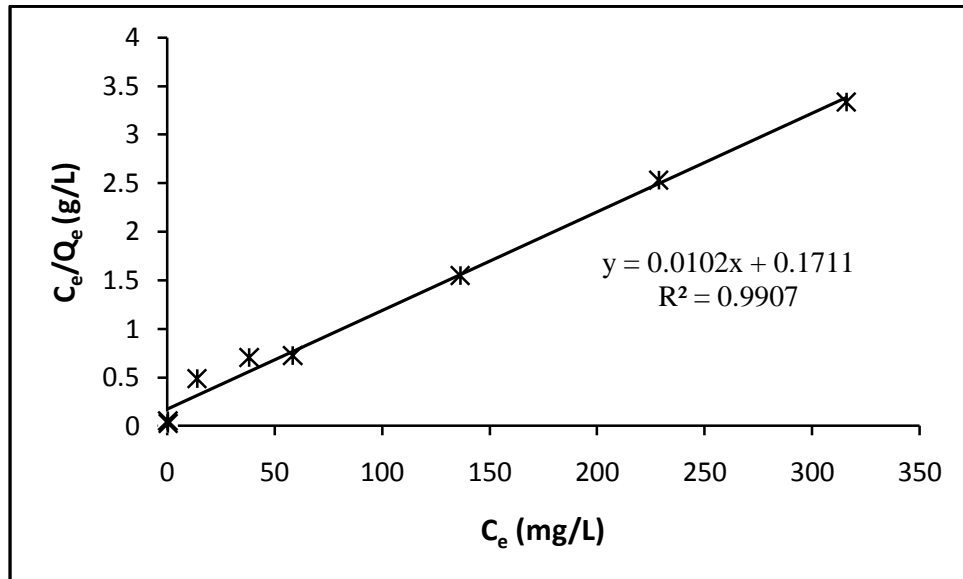


Figure 4.25: Linear plot of Langmuir Isotherm for B7 sample. [Conditions; adsorbent dose: 0.3000g; pH: 6; contact time: 6 hours; temperature: 25 °C; agitation rate = 180 rpm].

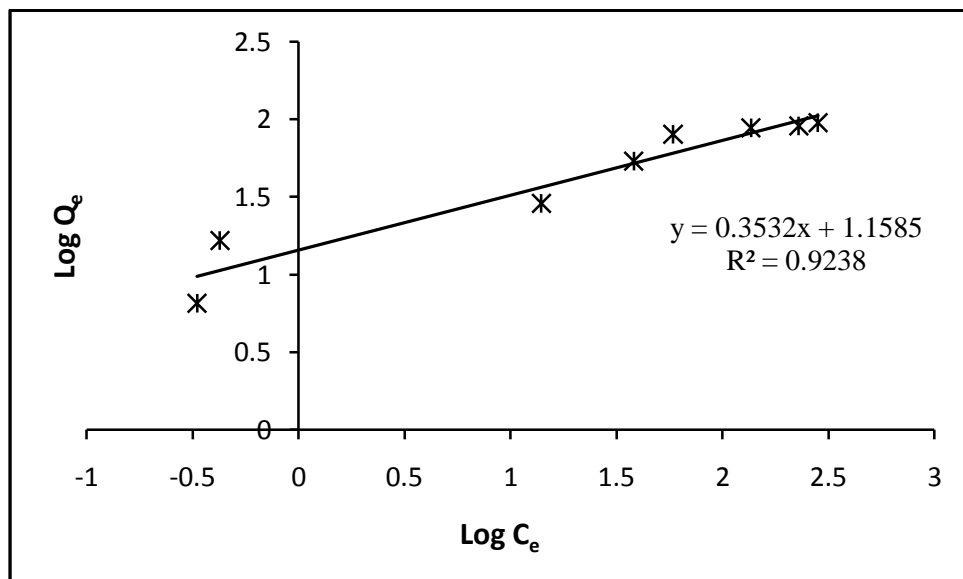


Figure 4.26: Linear plot of Freundlich Isotherm for B7 sample. [Conditions; adsorbent dose: 0.3000g; pH: 6; contact time: 6 hours; temperature: 25 °C; agitation rate = 180 rpm].

Figure 4.25 and 4.26 shows that the linear plots of Langmuir and Freundlich models both describes the B7 isotherm data well fitted with the correlation coefficient (R^2) value of 0.9907 and 0.9238, respectively. The maximum sorption capacity (q_m) of mercury ion onto B7 adsorbent sample calculated from Langmuir isotherm was 98.04 mg/g. The Langmuir constant R_L value of this system was 0.4561 ($0 < R_L < 1$ is favourable) which indicates that the favourable adsorption of mercury ion onto B7 adsorbent. As referred to R^2 value, the Langmuir generally fitted better than Freundlich model. This suggest that the complete monolayer adsorption of mercury ion on B7 adsorbent surface. The Freundlich constant, K_F observed the extent of 1.1585 mg/g mercury removal onto B7 adsorbent hence a measure of the maximum sorption capacity (q_m) by Langmuir model. The two Langmuir and Freundlich constants K_a and n for B7 have a highest value of 0.0596 and 2.8310 respectively, as compared to pristine MWCNTs and B10 adsorbent samples. The high value of n constant indicates a strong bond interaction between the B7 adsorbent and mercury ion. As reported by Okeola and Odebunmi, the value of n is >1 for adsorption of Methylene Blue onto activated carbon that indicates the strong bond between the adsorbate and adsorbent (Okeola & Odebunmi, 2010).

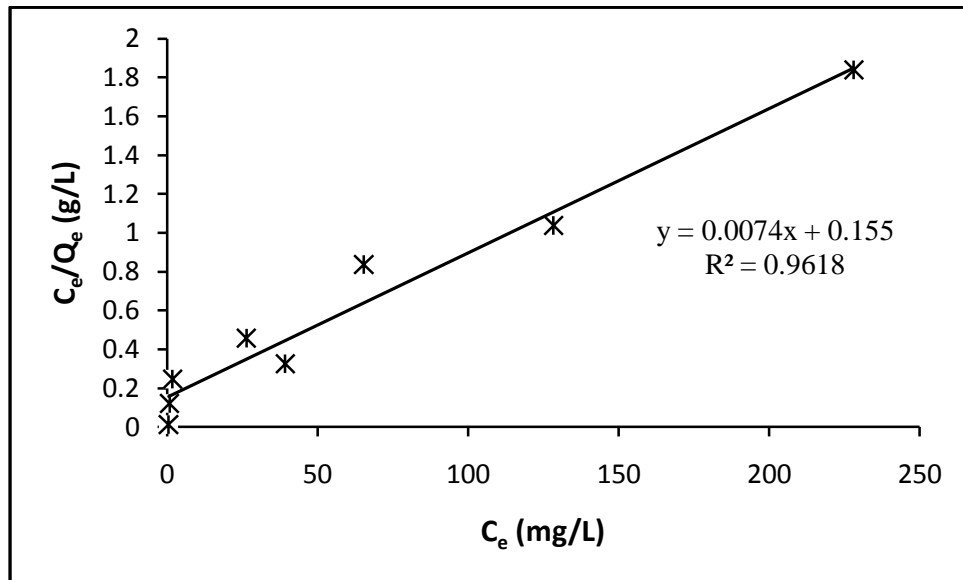


Figure 4.27: Linear plot of Langmuir Isotherm for B10 sample.
 [Conditions; adsorbent dose: 0.3000g; pH: 6; contact time: 6 hours;
 temperature: 25 °C; agitation rate = 180 rpm]

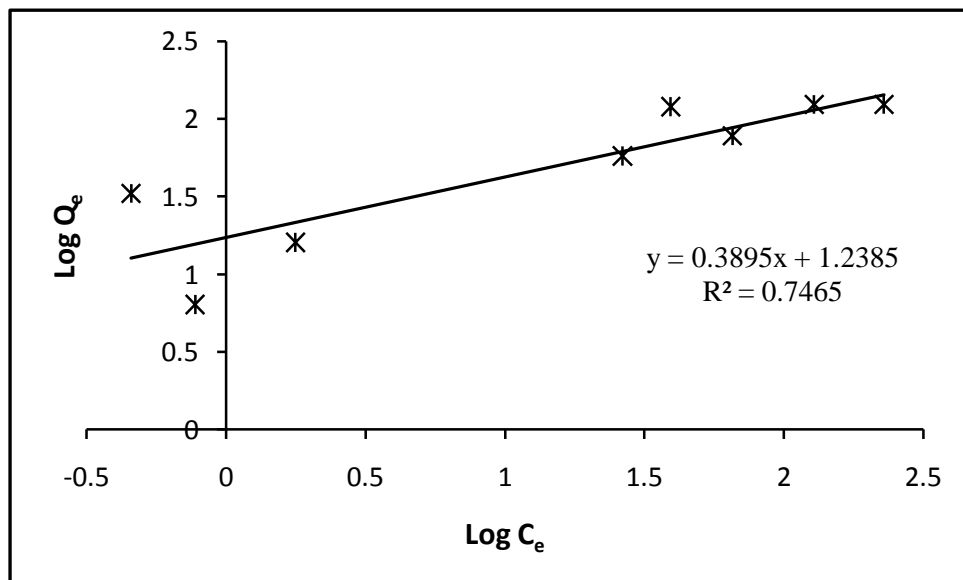


Figure 4.28: Linear plot of Freundlich Isotherm for B10 sample.
 [Conditions; adsorbent dose: 0.3000g; pH: 6; contact time: 6 hours;
 temperature: 25 °C; agitation rate = 180 rpm]

As shown in Figure 4.27, the linear plot of C_e/Q_e versus C_e adsorption of mercury ion onto B10 adsorbent obeys the Langmuir model with the correlation coefficient (R^2) value of 0.9616. The maximum sorption capacity of mercury ion onto B10 adsorbent was 135.04 mg/g. The Langmuir constant of R_L value of 0.5118 ($0 < R_L < 1$ is favourable) which indicates the favourable adsorption of mercury ion onto B10 adsorbent. But the experimental data poorly fitted the Freundlich isotherm with the correlation coefficient (R^2) value of 0.7465, see Figure 4.28. The results show that the Langmuir model fits the adsorption data better than the Freundlich model. The Freundlich model poorly fitted experimental data. Freundlich model shows the extent of adsorption capacity (K_F) value of 1.2385 mg/g from the maximum sorption capacity (q_m) by Langmuir model. The two Langmuir and Freundlich constants K_a and n for B10 have a value of 0.0477 and 2.5673 respectively. This n constant value for B10 is higher than n value for pristine MWCNTs but lower than n value for B7 adsorbent samples. This result shows that the B10 sample has middle interaction strength between mercury ions, as compared to pristine and B7 adsorbents.

All three (pristine, B7 and B10) adsorbent samples exhibit different type of adsorption behaviour characteristic. The pristine MWCNTs show the incomplete monolayer adsorption covered by mercury ion with poorly fitting Langmuir isotherm model. The B7 adsorbent shows excellent adsorption behaviour by obeying both Langmuir and Freundlich isotherms as compared to pristine MWCNTs and B10 adsorbent. This suggests complete monolayer adsorption and consequently the extent of the adsorption which might form a multilayer onto the B7 adsorbent. The B10 sample shows the complete monolayer adsorption behaviour as well fitted the Langmuir isotherm model with the highest maximum sorption capacity value of 135.04 mg/g as

compared to pristine MWCNTs and B7. Even the B7 has excellent adsorption behaviour by fitting well both to Langmuir and Freundlich isotherm but it has lower maximum sorption capacity, q_m (98.04 mg/g) compared to B10 adsorbent sample.